# A hydrothermal plume on the Southwest Indian Ridge revealed by a multi-proxy approach: Impact on iron and manganese distributions (GEOTRACES GS02)

Corentin Baudet, Eva Bucciarelli, Géraldine Sarthou, Cédric Boulart, Ewan Pelleter, Millie Goddard-Dwyer, Hannah Whitby, Rui Zhang, Ingrid Obernosterer, David Gonzalez-Santana, et al.

Marine Chemistry 265–266 (2024) 104401

Contents lists available at ScienceDirect

Marine Chemistry

journal homepage: www.elsevier.com/locate/marchem

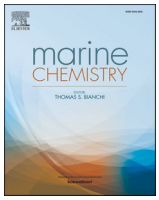

# A hydrothermal plume on the Southwest Indian Ridge revealed by a multi-proxy approach: Impact on iron and manganese distributions (GEOTRACES GS02)

Corentin Baudet [a,*], Eva Bucciarelli [a,1], Géraldine Sarthou [a,1], Cédric Boulart [b], Ewan Pelleter [c], Millie Goddard-Dwyer [d], Hannah Whitby [d], Rui Zhang [e], Ingrid Obernosterer [e], David Gonzalez-Santana [a,f], Morgane Léon [g], Pieter van Beek [g], Virginie Sanial [h], Catherine Jeandel [g], Frédéric Vivier [i], Maria-Elena Vorrath [j], Wen-Hsuan Liao [a,k], Yoan Germain [c], Hélène Planquette [a,*,1]

[a] Univ Brest, CNRS, IRD, Ifremer, LEMAR, IUEM, F-29280 Plouzané, France
[b] UMR 7144 AD2M, CNRS, Sorbonne Université, Station Biologique de Roscoff, 29680 Roscoff, France
[c] IFREMER, CNRS, Univ Brest, UBS, UMR6538, Laboratoire Geo-Ocean, F-29280 Plouzane, France
[d] Department of Earth, Ocean and Ecological Sciences, University of Liverpool, L69 3GP, UK
[e] CNRS, Sorbonne Université, Laboratoire d'Océanographie Microbienne, LOMIC, F-66650 Banyuls/mer, France
[f] Instituto de Oceanografía y Cambio Global (IOCAG), Universidad de Las Palmas de Gran Canaria, Spain
[g] LEGOS (CNRS, CNES, IRD, UPS, Université de Toulouse) 14 avenue Edouard Belin, 31400 Toulouse, France
[h] Université de Toulon, Aix Marseille Univ., CNRS, IRD, MIO, Toulon, France
[i] LOCEAN-IPSL, CNRS, Sorbonne Université, Paris, France
[j] Institute for Geology, University Hamburg, Germany
[k] Department of Earth Sciences, National Cheng Kung University, Tainan, Taiwan

## ARTICLE INFO

*Keywords:*
GEOTRACES
Southwest Indian Ridge (SWIR)
Hydrothermal sources
iron and manganese

## ABSTRACT

Iron (Fe) and manganese (Mn) are crucial micronutrients that limit oceanic primary productivity in the Southern Ocean. It has been recently suggested that hydrothermal activity may be an important source of oceanic dissolved iron, yet, this contribution is still not fully understood and only one active hydrothermal site has been reported on the Southwest Indian Ridge (SWIR), south of 40°S.

Using a multi-proxy approach, this study demonstrates the occurrence of hydrothermal venting on the SWIR in the near vicinity of the location 44°51.690 S, 36°10.460 E, which is likely to be a low or moderately high temperature fluid. Indeed, we report high values of dissolved methane to manganese ratios (up to 11.1 ± 1.2 mol $mol^{-1}$), low particulate iron (pFe) and manganese (pMn) concentrations (with maximum values of 0.7 nmol $L^{-1}$ and 0.06 nmol $L^{-1}$, respectively) associated with the presence of few oxyhydroxides, as well as high $^{223}$Radium (Ra) and $^{224}$Ra activities near the seafloor. The Fe and Mn data revealed a significant enrichment at depths influenced by hydrothermal circulation on the seafloor, within the Upper Circumpolar Deep Water. Dissolved Fe (dFe) and dissolved Mn (dMn) concentrations were enriched by 3- and 7-fold, respectively, and pFe and pMn by 2- and 1.5-fold, respectively, compared to a reference station located outside the SWIR. They were however lower than concentrations reported so far near high temperature vents, suggesting a weaker influence of this hydrothermal system on deep Fe and Mn reservoirs. We show that a large fraction of the dFe could be stabilized by organic complexation with humic substances (eHS, estimated 27–60% of dFe). High prokaryotic abundance related to the proximity of the hydrothermal vent suggests that other Fe-complexing ligands of biological origin might also stabilize Fe in its dissolved form. Collectively, these measurements integrated within the concept of a "multi-proxy approach", helped painting a more detailed picture of the complex interactions and processes in this region of the SWIR. Although the system is a source of both dFe and dMn to the deep ocean, the

* Corresponding authors at: UMR 6539/LEMAR/IUEM, Technopôle Brest Iroise, Place Nicolas Copernic, 29280 Plouzané, France.
*E-mail addresses:* corentin.baudet@univ-brest.fr (C. Baudet), helene.planquette@univ-brest.fr (H. Planquette).
[1] These authors contributed equally.

https://doi.org/10.1016/j.marchem.2024.104401
Received 21 April 2023; Received in revised form 25 January 2024; Accepted 13 May 2024
Available online 26 May 2024

low current velocities and the bathymetry likely limit the fertilization of surface water by dFe and dMn along this section of the SWIR.

## 1. Introduction

Iron (Fe) and manganese (Mn) are essential for cellular metabolisms (Sunda, 2012), and their low concentrations limit oceanic primary productivity and the structure of marine ecosystems in high nutrient low chlorophyll areas (HNLC) like the Southern Ocean (Boyd and Ellwood, 2010; Browning et al., 2021; Latour et al., 2021; Tagliabue et al., 2017). The study of the different sources of Fe and Mn to the ocean is therefore warranted to understand the functioning of oceanic ecosystems and the major biogeochemical cycles, including that of carbon. Among the different sources, the hydrothermal contribution is still poorly understood.

Since their discovery in the 1970s (Corliss et al., 1979), hydrothermal vents have been discovered in all oceanic basins and in different geodynamical settings (e.g. mid-ocean ridge, back-arc basin, arc setting), and have been surveyed for chemical, geological and biological interests (Beaulieu et al., 2015). Relative to seawater, hydrothermal fluids are enriched in metals, including Fe and Mn, whose concentrations vary considerably, with average values of 1970 ± 4510 μmol $L^{-1}$ ($n$ = 747) and 500 ± 714 μmol $L^{-1}$ ($n$ = 756), respectively (data compilation of hydrothermal vents sites on all major geologic structures in the world ocean; Diehl and Bach, 2020). The fluid composition depends on the water-rock interactions, the phase separation between the brine and the vapor phase enriched in gasses and finally the degassing processes (German and Seyfried, 2014; Shock, 1992; Von Damm, 1990). Schematically, two systems of hydrothermal vents can be distinguished according to the temperature of the fluid (i.e., high >300 °C and low <226 °C) as well as according to geochemical interactions (German et al., 2022). Magmatic systems are produced by eruptions of magma chambers containing molten rocks (basaltic and/or gabbroic), whereas ultramafic systems are produced by geochemical reactions that take place off-axis of the ridge, where seawater invades the oceanic crust through fissures (Martin et al., 2008).

Over the last decade, it has been demonstrated that dFe and dMn were persistent enough in hydrothermal plumes to be transported over thousands of kilometers in deep waters of the ocean (Fitzsimmons et al., 2014, 2017; Resing et al., 2015; Tagliabue et al., 2022) due to their physical (colloids) and chemical (ligand bound) speciation. Dissolved Fe and Mn from hydrothermal vents were indeed found to be associated with organic ligands, which maintain these elements in the dissolved phase above their oceanic limit of solubility (Bennett et al., 2008; Hawkes et al., 2013; Luther et al., 1992; Oldham et al., 2017; Sander and Koschinsky, 2011; Thibault de Chanvalon et al., 2023).

The latest estimation of high temperature hydrothermal vent contribution of Fe to the deep ocean is 4 ± 1 Gmol Fe $yr^{-1}$ (Resing et al., 2015) with only 0.12 ± 0.07 Gmol Fe $yr^{-1}$ from these hydrothermal sources possibly reaching the surface ocean (Roshan et al., 2020). This is considered to be minor compared to atmospheric or resuspended sediment supply at the global scale (Aumont and Bopp, 2006; Moore and Braucher, 2008; Roshan et al., 2020), but may be significant in the Southern Ocean where advected hydrothermal dFe supply to surface waters is almost equivalent to the supply of Fe from dust deposition (Baker, 2017; Resing et al., 2015; Roshan et al., 2020). Recent studies have indeed linked this hydrothermal Fe supply into surface waters to large Southern Ocean phytoplankton blooms (Ardyna et al., 2019; Moreau et al., 2023; Schine et al., 2021; Tagliabue and Resing, 2016). For Mn, hydrothermal inputs to the deep ocean are estimated to be 102 Gmol $yr^{-1}$ which is higher than other sources (van Hulten et al., 2017). However, the potential impact of enrichment by hydrothermal Mn on surface marine productivity has not been investigated so far, and overall, the influence of hydrothermal inputs on Fe and Mn distributions in the Southern Ocean remain scarce.

Based on the assumption that the low magmatic budget of slow-spreading ridges (20–55 mm $yr^{-1}$) have a smaller impact on the ocean Fe budget, slow spreading ridges have been less studied than the fast-spreading ridges (80–140 mm $yr^{-1}$) (Beaulieu et al., 2015). Yet, recent studies suggest that hydrothermal systems at slow and ultra-slow spreading ridge settings are more abundant than previously known (e.g. Baker, 2017). In slow and ultra-slow ridge settings, two types of hydrothermal systems can be distinguished: (1) mafic-hosted (Menez Gwen, TAG, Longqi, Logatchev, Saldanha) and (2) ultramafic-hosted (Lost City, Rainbow, Ashadze) hydrothermal systems (Fouquet et al., 2010; Wang et al., 2019). Ultramafic-hosted hydrothermal systems display a large diversity of type of venting (black smoker, medium to low-temperature fluids, low temperature diffuse fluids and fluid chemistry). The Southwest Indian Ridge (SWIR) is among the world's slowest ultraslow-spreading ridges (~14–16 mm $y^{-1}$, German et al., 1998; Sauter and Cannat, 2010). Along this ridge, the first active hydrothermal vent field was revealed in 2012 (Tao et al., 2012), and, to date, about 30 active hydrothermal vents are now inventoried according to InterRidge data (red stars on Fig. 1) (Bach et al., 2002; Baker et al., 2004; Cannat et al., 2021; German et al., 1998; Han et al., 2010; Lecoeuvre et al., 2021; Tao et al., 2009, 2014). However, few studies investigated their Fe and Mn inputs to the deep water masses (Fang and Wang, 2021; Wang et al., 2019). Between Prince Edward (35°E) and Eric Simpson (40°E) fracture zones, the presence of hydrothermal vents was suspected from bathymetry, magnetism and gravity data during the SWIFT cruise in 2001 (Humler, 2001; Sato et al., 2013 as delimited by the red line on Fig. 1b). As part of the GEOTRACES international program, the SWINGS cruise (GEOTRACES GS02 section) was designed to sample a variety of provinces, from South Africa to Heard Island (Fig. 1a), and dedicated some time to hydrothermal exploration along the SWIR to investigate if this could be an important source of iron and manganese. Following a bathymetric survey (doi: 10.17882/89462; Fig. 1c), station 14 located between a magmatic and a low magmatic activity segment (PE-1 in Sato et al., 2013; red line Fig. 1b) was investigated. In this study, we demonstrate the presence of hydrothermal activity at station 14 using methane ($CH_4$) and dMn, then we further characterize the type of hydrothermal system before discussing its implications for Fe and Mn distributions using an interdisciplinary approach (chemistry, geology and biology).

## 2. Methods

### 2.1. Study area

The South West Indian GEOTRACES Section (SWINGS; section GS02, PIs Hélène Planquette and Catherine Jeandel) took place on the N/O Marion-Dufresne, from January 11th to March 8th, 2021.

After 25 h of bathymetric survey on the SWIR on an area of around 200 $km^2$ (Fig. 1), station 14 (36.174°E; 44.862°S, bottom depth = 1395 m) was sampled for $CH_4$, trace metals, prokaryotic abundance, and Ra isotopes to trace a potential hydrothermal vent. Station 14 is located between a magmatic section to the west and a low magmatic section to the east according to the geophysical survey from Sato et al. (2013) (red box; Fig. 1). This station was compared with another station nearby, station 16 (36.111°E; 46.507°S, bottom depth = 2633 m; Fig. 1), which was not located on the SWIR and therefore considered as a reference station. Samples for trace metals, humic ligands and bacterial abundance were collected at stations 14 and 16.

### 2.2. Hydrographic data

Conductivity-temperature-depth (CTD) data were collected from a Seabird SBE911 plus probe, equipping both the clean and standard rosettes, with an accuracy of ± 0.001 °C for temperature and ± 0.003 mS $cm^{-1}$ for conductivity. Dissolved oxygen concentration ($O_2$) was retrieved from a Seabird SBE43 sensor attached to each rosette. Potential temperature (θ), salinity (S), and $O_2$ data were used to characterize the different water masses. Temperature and conductivity sensors were calibrated postcruise by SeaBird and regular salinity calibrations were done on board, leading to a correction of +0.005 for salinity. Likewise, dissolved oxygen data were further calibrated with ex-situ titrations (Winkler method) from water samples taken at most stations.

### 2.3. $CH_4$ analyses

Samples for dissolved $CH_4$ analysis were collected in 20 mL headspace glass vials directly from the Niskin bottles, poisoned with 20 μL of saturated $HgCl_2$ solution to inhibit any microbial activity, and sealed using gas-tight septa (20 mm, grey butyl-rubber) and aluminum crimp caps. All samples were stored at 4 °C until analysis on shore. Dissolved $CH_4$ concentrations were determined by gas chromatography analysis after headspace extraction (Kolb and Ettre, 1997), using a Shimadzu Headspace Sampler (HS-20) connected to a Gas Chromatograph (Shimadzu GC-2030) fitted with a barrier discharge ionization detector (BID) and a 30 m SH-Rt-Msieve 5 A column. With this set-up, headspace extraction was entirely automated: pressurization of the sample up to 2 bars, heating at 90 °C and equilibration for 10 min. Then, an aliquot of the gas sample was transferred to a 1 mL injection loop, maintained at 150 °C and injected into the column maintained at 40 °C. The detection

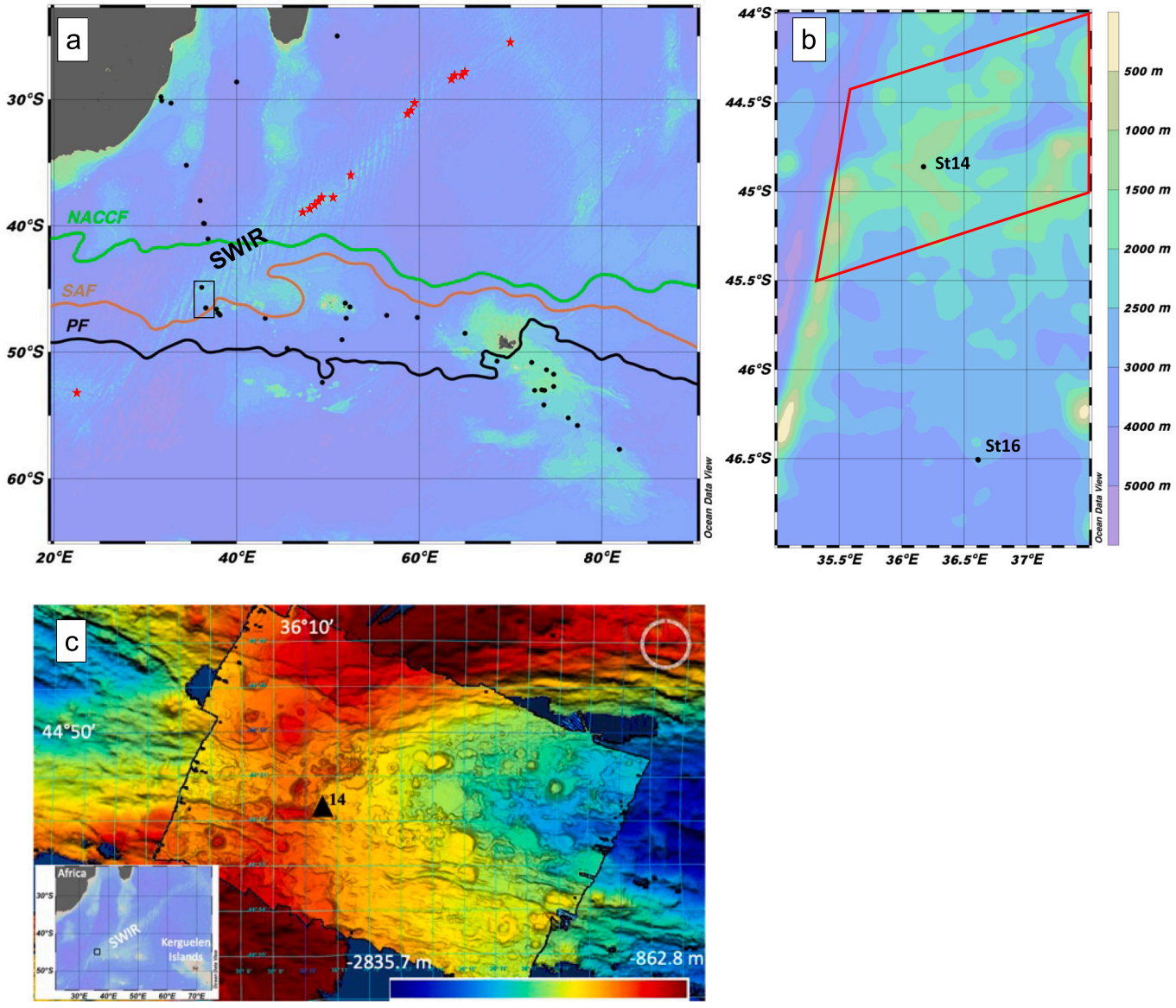


**Fig. 1.** (a) Bathymetry map showing the location of the stations sampled for trace metals (black dots) during the SWINGS cruise (GEOTRACES GS02 section). The green, orange and black lines represent the North Boundary of the Antarctic Circumpolar Current (NBACC), the Subantarctic Front (SAF) and the Polar Front (PF), respectively, according to Park et al. (2019). The red stars represent the active hydrothermal vents reported so far on the SWIR (data from the InterRidge Vent database: https://vents-data.interridge.org/ventfields-osm-map). (b) Close-up on stations 14 (SWIR) and 16 (Reference), the red line delimits the geophysical survey PE-1 realized in 2008 by Sato et al. (2013) and Humler (2001) (see Introduction). (c) High-resolution bathymetric map around station 14. (For interpretation of the references to colour in this figure legend, the reader is referred to the web version of this article.)

limit was 0.2 nmol $L^{-1}$ for dissolved $CH_4$.

### 2.4. Radium analyses

Acrylic cartridges impregnated with $MnO_2$ (Mn-cartridges) were mounted on McLane in-situ pumps (ISP) to preconcentrate in-situ dissolved radium (Ra) isotopes from large volumes of seawater (Henderson et al., 2013). Seawater first passed through Supor (0.8 μm pore size) or QMA (Whatman© 1 μm pore size) filters before passing through the Mn-cartridges. ISP were deployed at station 14 for 3 h of pumping, thus filtrating between 427 and 674 L of seawater. Both $^{223}Ra$ (half-life of 11.4 d) and $^{224}Ra$ (half-life of 3.66 d) activities were determined by performing several counting of Mn-cartridges on Radium Delayed Coincidence Counter (RaDeCC) systems (Moore, 2008). The Ra preconcentration efficiencies of the Mn-cartridges were determined for each sample. Further details on radium analysis can be found in Léon et al. (2024).

### 2.5. Trace metal sampling and analyses

GO-FLO bottles and all the sampling material were cleaned before the cruise following the GEOTRACES cookbook (Cutter et al., 2017). The trace metal clean rosette was deployed with a resolution of up to 24 depths per station. Immediately after recovery, the rosette was transferred into a clean container for sampling trace elements. Particle levels in the clean container atmosphere were controlled with a particle counter (Lighthouse HH3016) and when levels were adequate for ISO class 6 levels, sampling could begin. Bottles were pressurized with 0.2 μm-filtered nitrogen (Air Liquide®).

#### 2.5.1. Dissolved trace metals

Samples dedicated to dissolved trace metal (dMn and dFe) analyses were filtered on-line through a 0.45 μm polyethersulfone filter (Supor®) and collected in duplicates in acid-cleaned 60 mL LDPE bottles. All samples were acidified within 24 h of collection with hydrochloric acid (HCl, ultrapure grade, Merck, final pH 1.8), stored at room temperature, and analyzed 12 months later by inductively-coupled plasma mass spectrometry (ICP-MS).

The dFe and dMn concentrations were measured using the preconcentration system seaFAST-pico™ coupled to a high-resolution magnetic sector field inductively-coupled plasma mass spectrometer (SF-ICP-MS, Element XR – Pôle Spectrométrie Ocean, Brest) following Tonnard et al. (2020). Acidified MQ water with hydrochloric acid (HCl, ultrapure grade, Merck, 0.2‰, final pH 1.8, $n = 9$) was analyzed regularly but represents an upper end of the analytical blank. Therefore, the air blank (i.e., no sample taken up but with the contribution of all reagents) was used (dMn = 0.08 ± 0.04 nmol $L^{-1}$; dFe = 0.14 ± 0.05 nmol $L^{-1}$). All dMn and dFe data were above the detection limit (LOD), defined as three times the standard deviation (sd) of the air blank (LOD dMn = 0.010 nmol $L^{-1}$; LOD dFe = 0.041 nmol $L^{-1}$, $n = 23$). The reproducibility of our analyses has been verified with duplicates (n = 23; Coefficient of variation (CV) for dM$n$ = 5.4% and dFe = 8.0%) and the standard deviation of our values were estimated from the CV of the calibration coefficient. The standard deviation provided for dissolved Fe and Mn concentrations includes the errors associated with filtered volume of seawater, the number of counts per second provided by ICP-MS analysis, and the standard deviation of the calibration lines. Reference seawater (NASS-7, Nadeau et al., 2016) and GEOTRACES consensus (GSC and GSP) seawaters were used to certify the accuracy of our analyses (Table 1).

#### 2.5.2. Particulate trace metals

Suspended particles were collected on 25 mm diameter 0.45 μm polyethersulfone filters (Supor®). After collection, excess seawater was removed using a syringe then filters were placed in clean petri-slides and kept frozen at −20 °C until analysis back at the laboratory. Prior to acid digestion, 15 mL Teflon™ vials were cleaned with 6 mol $L^{-1}$ HCl (Fisher Scientific—Merck Suprapur grade) and heated at 130 °C for 4 h, then rinsed 3 times with Milli-Q water. Vials were then cleaned with 3 mL of a solution of 1.45 mol $L^{-1}$ HF (Fisher Scientific— Merck Suprapur Grade) and 8 mol $L^{-1}$ $HNO_3$ (Fisher Scientific—Suprapur Grade) for 4 h at 130 °C, then rinsed 5 times with Milli-Q water and dried under a laminar flow hood. All filters were digested with 2 mL of acid solution containing 8 mol $L^{-1}$ $HNO_3$ and 2.9 mol $L^{-1}$ HF (Fisher Scientific—Optima grade concentrated acids) for 4 h at 130 °C. Afterwards, the solution was evaporated to near dryness (dry down step) at 110 °C under an ISO 5 HEPA fume hood. The residue was redissolved with 400 μL of concentrated $HNO_3$ (Fisher Scientific—Optima grade) and evaporated again at 110 °C. Then, the new residue was dissolved in 3 mL of 3% (v/v) $HNO_3$ (Fisher Scientific—Optima grade) before being archived into precleaned 15 mL polypropylene tubes (Corning®) or 5 mL cryotubes (Trucool®) until analysis (Planquette and Sherrell, 2012). Before being analyzed, the archive solutions containing our samples were diluted (factor 10) in 3% (v/v) $HNO_3$ (Fisher Scientific—Optima grade) spiked with Indium (In) as an internal standard (~ 1 ppb, as run in final solution). Calibration curves, prepared gravimetrically in a 3% (v/v) $HNO_3$ solution (spiked at 1 ppb of In), were analyzed at the beginning, middle and end of each analytical session. Based on the recommendations by Planquette and Sherrell (2012), analyses were performed with a magnetic sector inductively coupled plasma mass spectrometer (SF-ICP-MS, Element XR – Pôle Spectrométrie Ocean, Brest) at medium resolutions ($^{55}Mn$; $^{56}Fe$). A total of 44 process blank filters, i.e., 1 L of filtered seawater passing through a clean filter, were collected near the surface at nearly all stations sampled along the SWINGS transect ($n = 44$; pMn = 0.37 ± 0.23 ng/filter; pFe = 11 ± 7 ng/filter). The particulate data obtained were above the detection limit (defined as three times the standard deviation of the blank: pMn = 0.69 ng/filter; pFe = 21 ng/filter). Every 10 samples, duplicate measurements of samples were made in order to verify the precision of the method ($n = 45$; coefficient of variation pMn = 11%; CV pFe = 5%). The standard deviations provided for particulate metal concentrations include the errors associated with the filtered seawater volume, the scale deviation used to weigh the archive solutions, the number of counts per second provided by ICP-MS analysis, and the standard deviation of the calibration lines. Following the same acid digestion protocol, certified and consensus materials were analyzed (MESS-4 (Willie et al., 2014), PACS-3 (Willie et al., 2013), Bureau of Reference plankton certified reference material (BCR-414) and Arizona

**Table 1**
Measured dissolved (in nmol $L^{-1}$) and particulate (in mg $kg^{-1}$) Mn and Fe compared to the consensus and certified reference material values.

| | dMn (nmol $L^{-1}$) | | dFe (nmol $L^{-1}$) | |
|---|---|---|---|---|
| | Certified value | Measured value | Certified value | Measured value |
| NASS 7 (n = 10) | 13.46 ± 0.11 | 13.03 ± 0.82 | 6.15 ± 0.05 | 6.14 ± 0.49 |
| GSC ($n$ = 15) | 2.18 ± 0.08 | 1.87 ± 0.26 | 1.54 ± 0.12 | 1.87 ± 0.32 |
| GSP (n = 2) | 0.778 ± 0.034 | 0.647 ± 0.042 | 0.155 ± 0.045 | 0.184 ± 0.015 |

| | pMn (mg $kg^{-1}$) | | pFe (mg $kg^{-1}$) | |
|---|---|---|---|---|
| | Certified value | Measured value | Certified value | Measured value |
| MESS 4 (n = 5) | 298 ± 14 | 342 ± 31 | 37,900 ± 1600 | 37,178 ± 3300 |
| PACS 3 ($n$ = 3) | 432 ± 16 | 491 ± 97 | 41,060 ± 640 | 39,053 ± 7632 |
| BCR 414 (n = 3) | 299 ± 13 | 343 ± 20 | 1850 ± 190 | 2121 ± 118 |
| ATD (n = 3) | 728 ± nd | 813 ± 87 | 24,480 ± 10,491 | 29,851 ± 2548 |

Test Dust (Morton et al., 2013), Table 1).

### 2.6. Scanning electron microscopy

Particulate material has been characterized using FEI Quanta 200 scanning electron microscope (SEM) coupled with an OXFORD energy dispersive spectroscopy (EDS) X-MAX detector (80 $mm^2$). EDS imaging on a ca. 1 $mm^2$ filter surface (carbon-coated) was first made to detect Fe- and Mn- bearing minerals. Secondary electron images were acquired for textural characterization and additional EDS spot analyses were completed in order to identify the different mineral phases (e.g. oxy-hydroxides, oxides, silicates…). EDS analyses were performed at 20 kV and a 10 mm working distance. Secondary electron images were acquired at 5 kV.

### 2.7. Electroactive humic ligands

Samples for electroactive humic substances (eHS) were collected as for dFe in 60 mL acid-cleaned LDPE bottles then stored at −20 °C prior to analysis. Molybdenum (Mo) standard solutions were prepared by dilution of 1 g $L^{-1}$ Mo standard (BDH Spectrosol) in Milli-Q. Suwannee River Fulvic acid (SRFA) standards (2S101H, IHSS) were prepared by dissolving in Milli-Q. Samples and standards were acidified to pH 2 using Trace Metal grade HCl (Fisher Scientific). Analyses were conducted using cathodic stripping voltammetry as described in Pernet-Coudrier et al. (2013) using a Metrohm μAutolab 3 potentiostat, Metrohm IME663 and Metrohm V663 stand. The system consisted of a hanging mercury drop working electrode, a glassy carbon auxiliary electrode, and an Ag:AgCl (3 mol $L^{-1}$ KCl) reference electrode. Analyses took place inside an acid cleaned glass electrochemical cell. Modifications to the method described by Pernet-Coudrier et al. (2013) include purging the sample with nitrogen gas for 600 s, using a deposition time of 400 s, and using the 1st derivative of the smoothed peak processed in ECD software (Omanovic and Pizeta, 2016; ElectroChemical Data Software ECDSOFT) to quantify eHS.

We estimated the minimum and maximum eHS Fe binding capacity of our samples using the reported values of eHS standards in the literature as in Whitby et al. (2020). The minimum eHS Fe binding capacity is calculated using the Suwannee River Fulvic Acid (SRFA) standard Fe binding capacity (SRFA, 14.6 nM Fe $mg^{-1}$ SRFA; eq. 1) and the maximum eHS binding capacity is calculated from the (Suwanee River Humic Acid (SRHA) Fe binding capacity, (32 nM Fe $mg^{-1}$ SRHA; eq. 2) reported values of Fe binding capacity of eHS standards (Laglera and van den Berg, 2009; Sukekava et al., 2018), we estimated the minimum and maximum Fe eHS binding capacity of our samples, as in Whitby et al. (2020). Note, we elected to not include the standard deviations in the calculations, which is a modification to the original calculation proposed by Whitby et al. (2020). This was in order to minimise the size of the eHS Fe binding envelope to the lower limit.

$$SRFA\ minimum\ eHS\ Fe\ binding\ capacity = [eHS] \times 14.6 \quad (1)$$

$$SRFA\ maximum\ eHS\ Fe\ binding\ capacity = [eHS] \times 32 \quad (2)$$

### 2.8. Determination of prokaryotic abundance

For the enumeration of non-phototrophic prokaryotes by flow cytometry, 1.44 mL of unfiltered seawater were fixed with glutaraldehyde grade I 25% (1% final concentration), and incubated for 30 min at 4 °C, then quick-frozen in liquid nitrogen and stored at −80 °C until analysis. Counts were performed on a FACSCanto II flow cytometer (Becton Dickinson) equipped with 3 air-cooled lasers: blue (argon 488 nm), red (633 nm) and violet (407 nm). Cells were stained with SYBR Green I (Invitrogen – Molecular Probes) at 0.025% (vol/vol) final concentration for 15 min at room temperature in the dark. Stained prokaryotic cells were discriminated and enumerated according to their right-angle light scatter (SSC) and green fluorescence. Fluorescent beads (1.002 μm; Polysciences Europe) were systematically added to each analyzed sample as internal standard. The cell abundance was determined from the flow rate, which was calculated with TruCount beads (BD biosciences).

## 3. Results and discussion

### 3.1. Hydrographic settings

Similar water masses were observed at stations 14 and 16 (Fig. 2). The Antarctic Intermediate Water (AAIW; 3.2 °C < θ < 5 °C; S < 34.3; $[O_2]$ > 220 μmol $kg^{-1}$, Piola and Georgi, 1982; Wong, 2005) was located between 400 m and 800 m at station 14 and between 340 m and 790 m at station 16. The Upper Circumpolar Deep Water (UCDW; 2.6 °C < θ < 3.2 °C; 34.3 < S < 34.6; 180 μmol $kg^{-1}$ < $[O_2]$ < 220 μmol $kg^{-1}$) was located between 800 m and the bottom at station 14 and between 800 m and 1270 m at station 16. Below UCDW, the Lower Circumpolar Deep Water (LCDW; θ < 2.6 °C; S > 34.6; $[O_2]$ > 180 μmol $kg^{-1}$) was present down to the bottom at station 16 (Gordon, 1975; Zu et al., 2022). The boundary between the AAIW, UCDW and LCDW layers was determined from a neutral density criterion of 27.5 kg $m^{-3}$ and 27.8 kg $m^{-3}$, respectively.

### 3.2. Hydrothermal vent detection

During this cruise, we measured $CH_4$ and dissolved Mn concentrations (Fig. 3), both being tracers of hydrothermal vents (Charlou et al., 1996; Love et al., 2008).

Within UCDW, at station 14, $CH_4$ concentrations ranged from 3.8 ± 0.2 nmol $L^{-1}$ at 1101 m depth to 7.5 ± 0.4 nmol $L^{-1}$ at 1282 m depth, which are significantly higher than the typical background concentration of below 1 nmol $L^{-1}$ (Reeburgh, 2007). Concentrations of dMn ranged between 0.22 ± 0.02 nmol $L^{-1}$ and 0.30 ± 0.03 nmol $L^{-1}$ in AAIW, then increased in UCDW to a maximum of 1.17 ± 0.11 nmol $L^{-1}$ at 1300 m (Fig. 3). In contrast, dMn concentrations at station 16 remained fairly constant throughout the whole water column (0.15 ± 0.06 nmol $L^{-1}$; Fig. 3 and Supplementary Table 1). The dMn and $CH_4$ concentrations were significantly correlated in UCDW at station 14 (Pearson's correlation; $R^2 = 0.81$; $p$-value = 0.027; $n = 7$).

At station 14, more investigations were conducted to better identify the origin of the $CH_4$ and dMn enrichments. Scanning electron microscopy (SEM) observations were performed in order to investigate the nature of particles collected at 1040 m, where dMn concentration was relatively low (0.48 ± 0.05 nmol $L^{-1}$) and at 1280 m, where dMn concentration was equal to 0.90 ± 0.09 nmol $L^{-1}$, close to its maximum. At 1040 m, we observed mixed particle aggregates of bio-detritus and lithogenic particles. The latter were composed of titanomagnetite (Fig. 4a), as indicated by a Ti enrichment associated with Fe-oxides, and of pyroxene and olivine minerals (Fig. 4b) as reflected by the Mg content in Fe-rich silicate particles which are the main Fe-bearing lithogenic phases. These minerals are of basaltic origin, which is in line with basalt dominated dredge contents reported by Zhou and Dick (2013) in the same area. No authigenic Fe or Mn oxides were observed at 1040 m.

At 1280 m, similar lithogenic particles were observed but SEM observations clearly revealed the presence of rare Fe and Mn oxyhydroxide particles suggesting authigenic precipitation of iron and manganese. As an example, Fig. 4C shows a Mn oxyhydroxide of 2.5 μm size located on a mixed particle aggregate, while Fig. 4D shows a quasi-spherical Fe oxyhydroxide of 2.5 μm diameter. Both spectra show as well the presence of phosphorus (P), that could be explained by removal of dissolved $PO_4$ from the plume and the water column by coprecipitation onto Fe-oxyhydroxides (Wheat et al., 1996).

At station 14 in UCDW, the correlation between $CH_4$ and dMn and the presence of Mn and Fe oxyhydroxides confirm that the station, located on the east flank of the SWIR, was impacted by hydrothermal

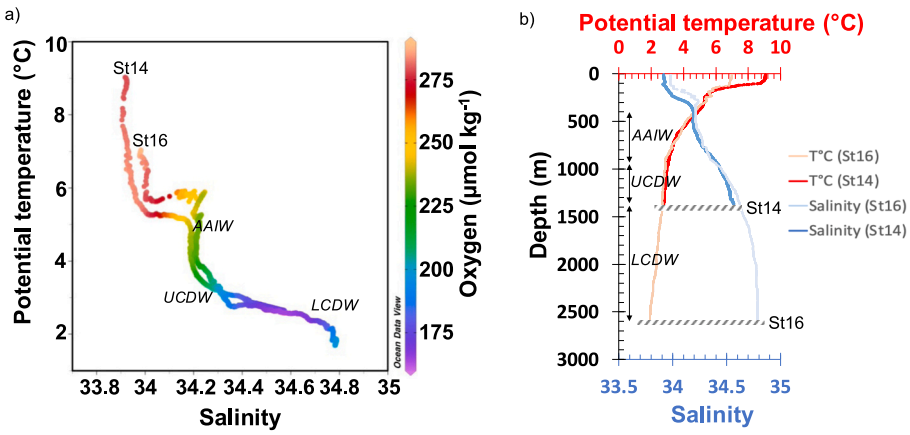


**Fig. 2.** a) Potential temperature vs salinity diagram for stations 14 and 16 between the surface and the seafloor (z axis represents the $O_2$ concentrations). b) Potential temperature (red) and salinity (blue) vertical profiles at stations 14 and 16. The dashed grey bars represent the seafloor. (For interpretation of the references to colour in this figure legend, the reader is referred to the web version of this article.)

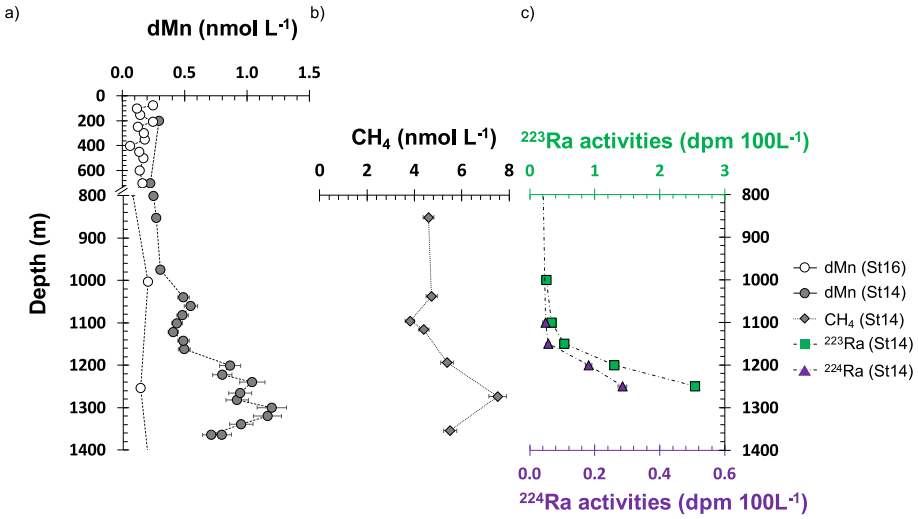


**Fig. 3.** Vertical profiles of a) dMn concentrations at station 14 (grey circles) and 16 (white circles). Note that two Go-Flos were triggered at 1340 m, hence two datapoints at this depth; b) $CH_4$ concentrations at station 14 (no $CH_4$ data available at station 16) and c) of $^{223}$Ra (green squares) and $^{226}$Ra (purple triangles) activities at station 14. All data are displayed with error bars that, at some depths, are smaller than the size of the symbols. Note that the y-axis is stretched between 800 m and 1400 m. The dashed grey bars represent the seafloor at station 14, which has been sampled at a higher resolution at depth than station 16, to better capture the variability of the nearby hydrothermal source. (For interpretation of the references to colour in this figure legend, the reader is referred to the web version of this article.)

activity on the seafloor (Bolton et al., 1988; German et al., 2022; Moorby et al., 1984; Murphy et al., 1991; Usui et al., 1986). The precise location remains, to date, unknown. High $^{224}$Ra (half-life of 3.66 days) and $^{223}$Ra (half-life of 11.3 days) activities were determined near the seafloor at station 14 (Fig. 3) and were attributed to hydrothermal activity (Léon et al., 2024). Both the short half-lives and the high activities of $^{224}$Ra and $^{223}$Ra, determined at station 14 and at nearby station 15 (located eastward of station 14 and which was not sampled for trace metals), suggest that these stations are located in the near vicinity of the source term. Based on a circulation model, as well as on physical and geochemical data, Léon et al. (2024) attempted to provide information on the location of the hydrothermal activity. A decrease in the $^{224}$Ra/$^{228}$Ra activity ratios was thus observed between stations 14 and 15 (ratios of 1.21 and 0.19, respectively), at a potential density of about 27.4 (corresponding to 1200 and 1250 m depth for station 14 and to 1160 and 1200 m depth for station 15). Assuming that stations 14 and 15 are impacted by the same source and considering an eastward-northeastward transport (i.e., from station 14 to station 15), Léon et al. (2024) estimated that the hydrothermal system is likely located within a ~ 3 km radius from station 14.

In the following section, we will investigate the distributions of particulate and dissolved Fe and Mn in the plume.

### 3.3. Biogeochemical characteristics of the hydrothermal source

#### 3.3.1. Distributions of particulate Fe and Mn

Between 1200 and 1340 m, i.e., within the suspected hydrothermal plume (see previous paragraph 3.2), pFe and pMn concentrations ranged from 0.32 ± 0.03 to 0.69 ± 0.03 nmol $L^{-1}$ and from 0.037 ± 0.004 to 0.060 ± 0.005 nmol $L^{-1}$, respectively, which is similar to concentrations determined at reference station 16 within the same water mass (0.36 ± 0.05 nmol $L^{-1}$ and 0.040 ± 0.002 nmol $L^{-1}$ for pFe and pMn respectively) (Fig. 5).

#### 3.3.2. Distribution of the dissolved Fe and Mn

At reference station 16, the average dFe and dMn concentrations within UCDW were 0.46 ± 0.01 nmol $L^{-1}$ ($n = 2$) and 0.17 ± 0.04 nmol $L^{-1}$ (n = 2), respectively (Supplementary Table S1). They are similar to

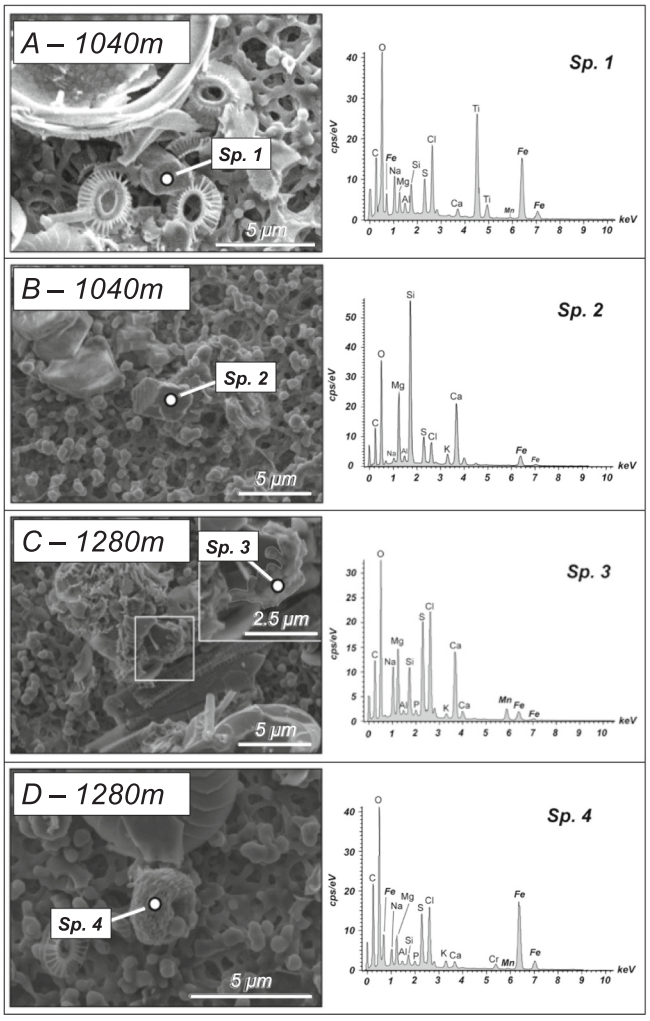


**Fig. 4.** Scanning electron microscopy (SEM) observations performed on filters collected at station 14. Electronic images were acquired at 5 kV with a scale of 5 µm and associated spectra were performed at 20 kV using the EDS X-MAX detector. Panels A and B show the presence of lithogenic particles collected at 1040 m, outside the hydrothermal signal, with associated marked site spectra (Sp.) 1 & 2 typical of lithogenic particles. Panels C and D show particles collected at 1280 m, under the influence of the hydrothermal signal. These particles are composed of Fe-oxyhydroxide particles as revealed by the associated marked site Sp. 3 & 4.

dFe concentrations in the Indian Sub-Antarctic UCDW (0.22 to 0.42 nmol $L^{-1}$, Tagliabue et al., 2012), and to dMn concentrations in the deep ocean that are reported to be lower than 0.2 nmol $L^{-1}$ (Browning et al., 2021; van Hulten et al., 2017). These values are also consistent with dFe and dMn concentrations measured in UCDW at 6 other SWINGS deep stations located between Durban and Marion and Prince Edward Islands (dFe =0.56 ± 0.17 nmol $L^{-1}$, $n = 7$, and dMn = 0.20 ± 0.06 nmol $L^{-1}$, $n = 8$, Baudet et al., in prep.).

At station 14, dissolved Fe concentrations ranged from 0.77 ± 0.09 nmol $L^{-1}$ at 800 m to 1.42 ± 0.16 nmol $L^{-1}$ at 1364 m (mean value: 1.10 ± 0.16 nmol $L^{-1}$, $n = 19$, Fig. 5). Like dFe, dMn reached high concentrations at station 14 (0.66 ± 0.29 nmol $L^{-1}$, $n = 20$), with a maximum of 1.17 ± 0.11 nmol $L^{-1}$ at 1300 m. These values are significantly higher (*t*-test, $p < 0.05$) than those measured within UCDW at the other deep stations mentioned above, including station 16 (dFe = 0.54 ± 0.15 nmol $L^{-1}$, $n = 9$, and dMn = 0.19 ± 0.06 nmol $L^{-1}$, $n = 10$, Baudet et al., in prep.).

We observed a different behavior between Fe and Mn in UCDW (Fig. 5). Dissolved Fe accounted for 70 ± 4% of total Fe (tFe = pFe + dFe), whereas dMn accounted for 92 ± 4% of total Mn (tMn = pMn + dMn). This difference could be explained by the proximity of the hydrothermal source. Due to the slower oxidation kinetics of Mn than of Fe, Mn oxyhydroxides are formed when moving away from the hydrothermal vent field, contrary to Fe oxyhydroxides which are formed near the source (Cave et al., 2002). Nevertheless, it is important to note that in some systems, Mn and Fe removal rates have been shown to be similar (e.g., Gartman and Findlay, 2020).

### 3.3.3. *Hypothesis on the nature of the hydrothermal source*

The correlation between $CH_4$ and dMn, as well as the Ra activities (Léon et al., 2024) confirmed that station 14 was impacted by a hydrothermal source, possibly located about 3 km away from the vent. With different distance-to-vent scales and different host rock influence between systems, it is difficult to make a direct comparison between this study and other systems. Nevertheless, our pFe and pMn concentrations were much lower than reported in the vicinity (maximum 100 m) of high temperature hydrothermal vents where concentrations ranged from 7 nmol $L^{-1}$ to 450 nmol $L^{-1}$ for pFe and 0.1 nmol $L^{-1}$ to 10 nmol $L^{-1}$ for pMn (Table 2). Between 7 and 10 km from Kemp Caldera and TAG, pFe concentrations were around 10 times higher than in our study, and up to 100 times higher on the East Pacific Rise (EPR 15°S) at a distance of 100 km from the vent (Table 2). In addition, we can highlight that the concentrations of dFe and dMn at proximity to the vents are higher near high-temperature (>300 °C) hydrothermal vents (varying from 12 nmol $L^{-1}$ to 223 nmol $L^{-1}$ for dFe and 15 nmol $L^{-1}$ to 122 nmol $L^{-1}$ for dMn, Table 2) than what we measured at station 14. The fact that our particulate and dissolved trace metal concentrations are low, despite the proximity to the potential source, suggests that the hydrothermal source is unlikely a high-temperature hydrothermal vent (i.e., >300 °C). We thus advocate that the hydrothermal plume is related to medium- (100–300 °C) to low-temperature (<100 °C) hydrothermal fluids.

In addition, the near-conservativity of $CH_4$ and dMn in the vicinity of hydrothermal sources allows us to use the $CH_4$:dMn ratios to better characterize the type of hydrothermal environment impacting station 14 (German et al., 2010, 2022). Indeed, mafic-hosted high temperature (>300 °C) hydrothermal fields generally exhibit low $CH_4$:dMn ratios (<0.3 mol $mol^{-1}$) (German et al., 2022). In contrast, ultramafic-hosted hydrothermal fields on slow ridges are exceptionally enriched in dissolved $CH_4$ (Charlou et al., 2002), leading to high $CH_4$:dMn ratios, ranging from 0.5 mol $mol^{-1}$ to 7.1 mol $mol^{-1}$ for plumes associated to ultramafic-hosted high temperature (>300 °C) vents and up to 30 mol $mol^{-1}$ for plumes related to lower temperature (<226 °C) vents (German et al., 2022). Within the hydrothermally-influenced UCDW waters, our $CH_4$:dMn ratios ranged from 6.4 ± 0.7 mol $mol^{-1}$ to 11.1 ± 1.2 mol $mol^{-1}$, suggesting that the hydrothermal source could be under an ultramafic influence (German et al., 2022). Another ultramafic system has already been observed on the SWIR ("Old City" located at 64.356°E; 27.506°S, Cannat et al., 2021; Lecoeuvre et al., 2021). However, station 14 is located on a magmatic segment and if the source is in the center of the segment, the geochemical interactions are controlled by mafic rocks. There is indeed an example situated at 37.15°N on the Mid Atlantic Ridge, such as "Lucky Strike" which is a mafic-hosted system showing a $CH_4$:dMn ratio of 3.8 ± 0.9 mol $mol^{-1}$ (German et al., 2022). Unfortunately, we cannot precisely determine the location of the hydrothermal source, so it is impossible to conclude on the exact nature of the source. Further study is necessary to characterize the exact nature of this hydrothermal source. Our physical (size fractionation) and organic speciation data, described below, will help to gain a better understanding of the influence of these hydrothermal plumes on the deep ocean cycling of Fe and Mn.

### 3.4. *Dissolved Fe stabilization by organic speciation*

The complexation of Fe to organic ligands is an important

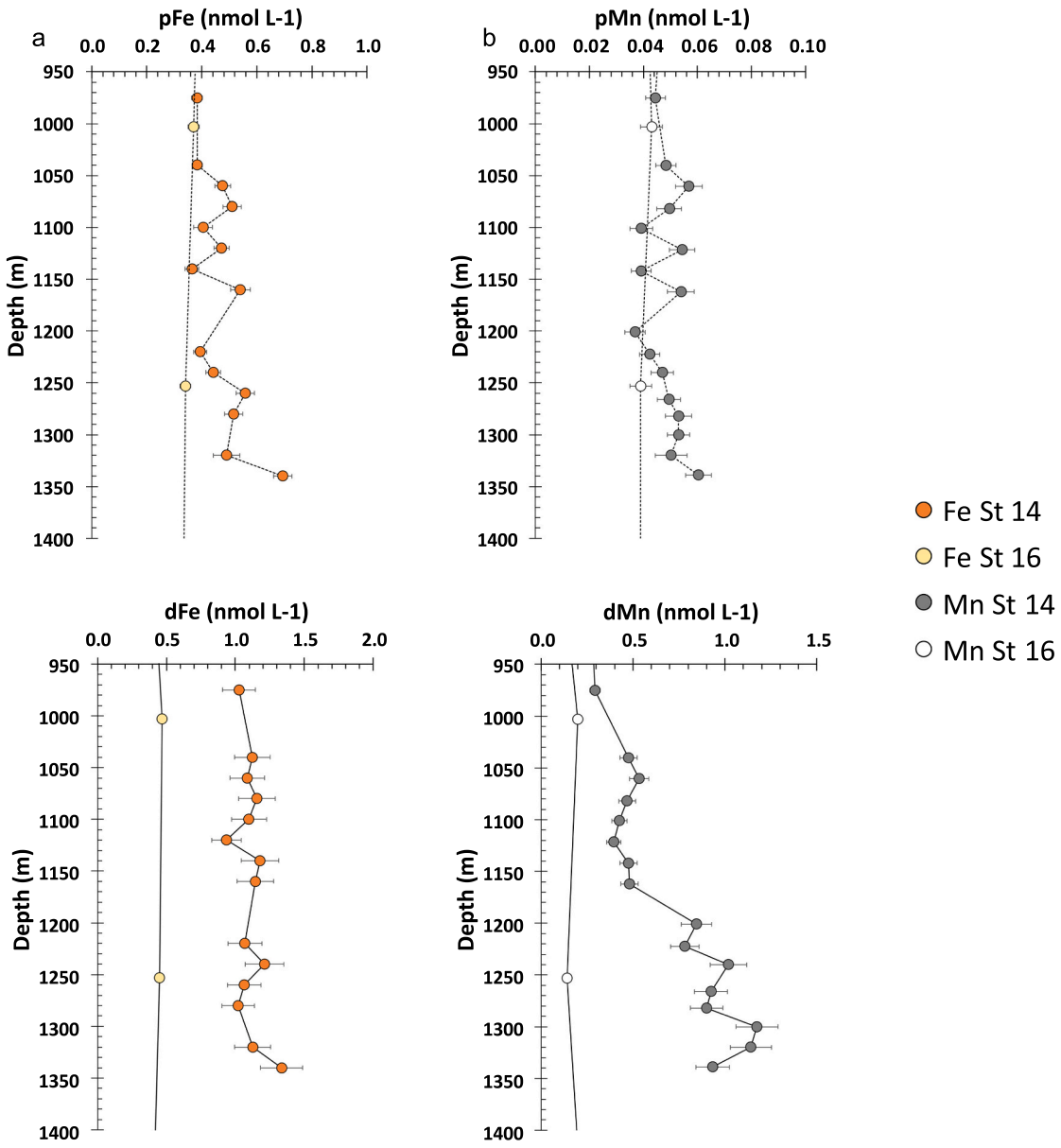


**Fig. 5.** Water column profiles at stations 15 and 16 in the UCDW (between 950 m and 1400 m) of dissolved Fe (dFe), particulate Fe (pFe), dissolved Mn (dMn) and particulate Mn (pMn). Station 14 has been sampled at a higher resolution at depth than station 16, to better capture the variability of the nearby hydrothermal source.

mechanism stabilizing hydrothermal Fe (Sander and Koschinsky, 2011). Iron-binding organic ligands have been observed in elevated concentrations in hydrothermal plumes compared to background seawater (Bennett et al., 2008; Hawkes et al., 2013; Hoffman et al., 2023). Iron binding organic ligands include siderophores, porphyrin, exopolymer like substances (EPS), and humic substances (Hassler et al., 2017). In this study, we measured electroactive humic substances (eHS), a heterogenous pool of organic matter which have been shown to play an important role in organic Fe complexation (Whitby et al., 2020; Yamashita et al., 2020).

We estimated the minimum and maximum Fe binding capacity of the eHS present using reported values for terrestrial standards SRFA and SRHA (Laglera and van den Berg, 2009; Sukekava et al., 2018). While marine HS in the upper water column is likely most similar to SRFA and thus would be expected to have the lower Fe-binding capacity, binding capacities are expected to change over time with DOM processing with little known effect of hydrothermal processes on humic metal complexation, so we report the full range of binding capacities (Whitby et al., 2020). At station 16 in UCDW, eHS had the capacity to bind on average 65% and potentially up to 100% of the dFe pool (Supplementary Table S1), consistent with previous observations in non-hydrothermally influenced water in other ocean basins (Whitby et al., 2020). At the hydrothermally influenced station, dFe concentrations were in excess of the eHS Fe binding capacity. Here, eHS were capable of complexing between 27 ± 6% to 60 ± 12% of dFe present (averaged in UCDW) (Fig. 6), within the range of bulk iron binding ligands observed in hot hydrothermal systems (30%, Hawkes et al., 2013).

However, there are several reasons why these values may be under- or over-estimated. Firstly, marine eHS likely have a range of Fe binding capacities that evolve with DOM processing, and therefore the binding capacities of the eHS estimated in this study may be different to terrestrial standards used for their quantification. This is particularly true for hydrothermally-altered humic material, which has not been studied in detail. Secondly, there could be competition for eHS Fe binding sites by other metals (e.g., Mn or Cu), particularly in metal-rich hydrothermal water (Abualhaija et al., 2015; Oldham et al., 2017;

**Table 2**
Comparative table of maximum concentrations (in nmol $L^{-1}$) of dissolved and particulate Mn and Fe (dMn, pMn, dFe, pFe), measured in seawater sampled in the vicinity of different types of hydrothermal systems under ultramafic or magmatic influences. SWIR = Southwest Indian Ridge; MAR = Mid Atlantic Ridge; CIR = Central Indian Ridge; ESR = East Scotia Ridge; EPR = East Pacific Rise.

| Source | Location | Latitude (°N) | Longitude (°E) | Full Spreading Rate (mm $yr^{-1}$) | Host rock | Maximal temperature fluid | Distance to the source (km) | dMn (nmol $L^{-1}$) | pMn (nmol $L^{-1}$) | dFe (nmol $L^{-1}$) | pFe (nmol $L^{-1}$) | Filter used | Reference |
|---|---|---|---|---|---|---|---|---|---|---|---|---|---|
| To be determined | SWIR | −44.862 | 36.174 | <20 | Ultramafic | | <0.1–3 | 1.2 | 0.06 | 1.4 | 0.7 | 0.45 µm polyethersulfone filters | This study |
| Lost City | MAR | 30.1250 | −42.1183 | 23 | Ultramafic | Low (90) | <0.1 | 0.2 | nd | 1.4 | nd | nd | Lough personnal communication |
| Rainbow | MAR | 36.2300 | −33.9020 | 21 | Ultramafic | High (362) | <0.1–10 | 60 - nd | nd | 33–2.8 | nd | 0.2 µm Sartobran 300 filter capsule | Lough et al., 2023 |
| TAG | MAR | 26.1367 | −44.8267 | 24 | Magmatic | High (369) | <0.1–10 | 71–1.5 | 0.12–0.06 | 90–2.1 | 150–5 | 0.2 µm Sartobran 300 filter capsule; 0.45 µm polyethersulfone filters | Lough et al., 2023; González-Santana et al., 2020 |
| Longqi | SWIR | −37.7838 | 49.6494 | 12 | Magmatic | High (379) | <1 | 63 | nd | 223 | nd | 0.2 µm polycarbonate membrane filter | Wang et al., 2019 |
| Edmond field | CIR | −23.8780 | 69.5960 | 48 | Magmatic | High (382) | <0.1 | 85 | 1 | 200 | 450 | 0.4 µm filter for pTM and < 0.1 µm for dTM (Whatman Cyclopore) | Sands et al., 2012 |
| E9N | ESR | −60.0500 | −29.9300 | 79 | Magmatic | High (380) | nd | nd | nd | 24–6.0 | nd | 0.2 µm polycarbonate membrane filter | Hawkes et al., 2013 |
| E2 | ESR | −56.0917 | −30.3250 | 66 | Magmatic | High (352) | nd | nd | nd | 80–20 | nd | 0.2 µm polycarbonate membrane filter | Hawkes et al., 2013 |
| Kemp Caldera | ESR | −59.7000 | −28.3166 | nd | Magmatic | High (nd) | <0.1–7 | 122–20 | 3.6–0.6 | 23–12.0 | 7.0–6.0 | 0.2 µm polycarbonate membrane filter | Hawkes et al., 2014 |
| EPR 15°S | EPR | −15.0000 | −112.7700 | 145 | Magmatic | High (nd) | <0.1–100 | 15–5.0 | 10–7.0 | 12–4.0 | 100–50 | 0.45 µm polyethersulfone filter; 0.2 µm Acropak Supor capsule filters | Fitzsimmons et al., 2017; Resing et al., 2015 |
| Carlsberg Ridge | IR | 3.7000 | 63.6666 | 30 | Ultramafic/ Magmatic | High (nd) | nd | 2.7 | nd | nd | nd | 0.45 µm filters | Ray et al., 2012 |

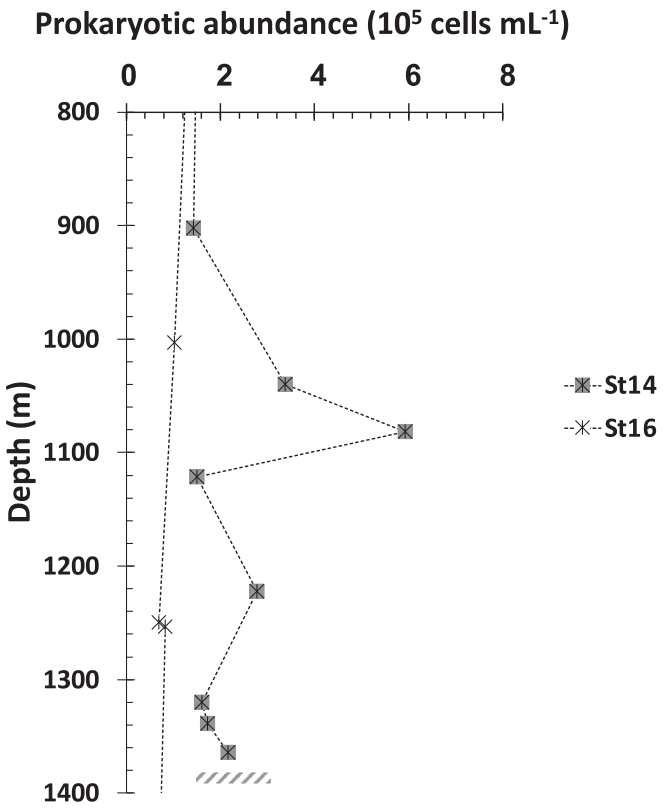


**Fig. 6.** Vertical profile of the prokaryotic abundance (cells mL$^{-1}$) at stations 14 (grey circles) and 16 (white circles) in the UCDW (800 m to 1400 m). Station 14 has been sampled at a higher resolution at depth than station 16, to better capture the variability of the nearby hydrothermal source. Note that the two bottles were triggered at 1266 m and 1267 m depth at Station 16.

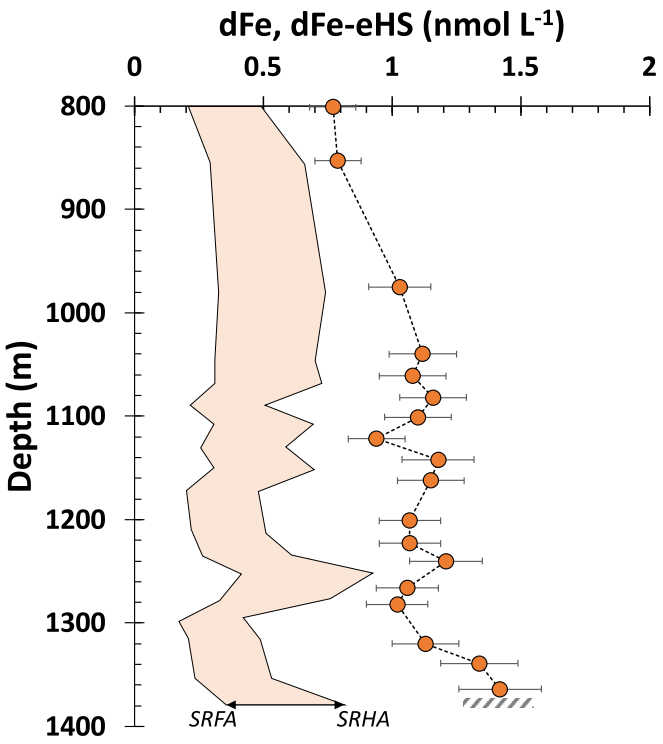


**Fig. 7.** Dissolved iron distribution within UCDW (between 800 m and 1400 m) at station 14 (dFe; orange circles) with an envelope (orange) for electroactive humic substances (eHS), encompassing the maximum (Suwannee River Humic Acid, SRHA) and minimum (Suwannee River Fulvic Acid, SRFA) iron-binding capacities reported for terrestrial IHSS standards (Laglera and van den Berg, 2009; Sukekava et al., 2018; Whitby et al., 2020).

Whitby and van den Berg, 2015). Thirdly it is unlikely that dFe is bound to eHS alone, because a portion of the dFe present is likely bound to other organic ligands such as porphyrin, exopolymer-like substances, and siderophores (Hassler et al., 2017). Hoffman et al. (2023) showed that siderophores can play an important role in stabilizing Fe along a 1700 km section of the Mid-Atlantic Ridge. Finally, some dFe may be contained in inorganic structures such as sulfide nanoparticles (Yücel et al., 2011).

The source of these eHS and siderophores is likely prokaryotic activity including vent associated thermogenic bacteria (Sarma et al., 2018), bacteria remineralizing vent produced organic matter (Cathalot et al., 2021), and/or abiotic formation of organic molecules (noted in ultramafic systems, Konn et al. (2009). Within UCDW at station 14, prokaryotic abundance (reaching 5.92 10$^5$ cells mL$^{-1}$ at 1080 m) was six times higher than at the reference station (1 10$^5$ cells mL$^{-1}$ at 1003 m; Fig. 7). General agreement between eHS concentration and prokaryotic abundance at station 14 support a possible role of prokaryotes in producing eHS and likely other unidentified iron binding organic ligands in this hydrothermal system.

We further determined the prokaryotic community composition using 16S rRNA gene sequencing at ~1300 m (1339 m at station 14 and 1250 m at station 16) (see Supplementary method 1). The communities were overall similar between sites, however we identified a few amplicon sequence variants (ASVs) with higher relative abundances at station 14 as compared to station 16 (Supplementary Fig. S1). Several of the ASVs that had higher relative abundances at station 14 as compared to station 16 in the particle-attached fraction belonged to *Pseudomonadales* (*Gammaproteobacteria*) while in the free-living fraction many belonged to *Nitrosopumilaceae (Thaumarchaeota*). Such a high abundance has already been observed near the "Old City" system, also located on the SWIR (Lecoeuvre et al., 2021). Many members belonging to *Pseudomonadales* are known siderophore producers (Palleroni, 2015) and have been shown to contain siderophore biosynthesis genes (Zhang et al., in revision) and express the respective transporters in the Southern Ocean (Debeljak et al., 2021). Metagenomic analysis (Supplementary methods 2; 3) revealed that at station 14 (Supplementary Fig. S2), the normalized gene abundances (genes per kilobase million, GPM) are about 3-fold (free-living) and 4-fold (particle-attached) higher as compared to the respective size fractions in 2 samples from the same water mass (UCDW) at different locations. This result indicates that there is a higher potential for siderophore biosynthesis at the hydrothermal vent station and this is particularly pronounced for prokaryotes attached to particles. The siderophores resulting from prokaryotic production could represent an additional mechanism for the stabilization of dFe at the hydrothermal vent station.

### 3.4.1. *Significance of the hydrothermal dFe source*

We found evidence that a portion of the hydrothermally derived dFe is likely stabilized by organic complexation. However, dFe concentrations remained low. Diffusive processes through overlying water masses could lead to small dFe enrichments (Léon et al., 2024), nevertheless, there is no topographic feature that could promote diapycnal transfer onto lighter isopycnals (Rintoul, 2018). This likely prevents any of this hydrothermally-sourced dFe from reaching the surface waters and contributing to the phytoplankton blooms observed in other studies above the SWIR (e.g., Ardyna et al., 2019; Moreau et al., 2023). This conclusion is in line with the recent conclusion of Tagliabue et al. (2022) stating that "while hydrothermal vents outside of surface ventilation and mixing hotspots are important for the interior ocean Fe cycle, they are unlikely to affect the upper ocean significantly, unless they are present at shallow depths".

### 3.5. Potential dissolved Mn source for the deep ocean

Recently, in addition to Fe, Mn availability was shown to play a key role in Southern Ocean productivity (Browning et al., 2021; Latour et al., 2021). The estimated dMn vertical flux (using the vertical eddy diffusion coefficients estimated from Ra and described in Léon et al. (2024) ranged from 133 ± 25 nmol $m^{-2}$ $d^{-1}$ to 350 ± 66 nmol $m^{-2}$ $d^{-1}$ between 1364 m and 975 m. The dMn flux is similar to the dFe flux ranging from 193 ± 70 nmol $m^{-2}$ $d^{-1}$ to 764 ± 353 nmol $m^{-2}$ $d^{-1}$ (Léon et al., 2024). In the literature, it has been reported that the effective hydrothermal Mn flux to the ocean interior was observed to be 25 times more important than the Fe flux (102 Gmol $yr^{-1}$ for Mn (van Hulten et al., 2017), vs 4 Gmol $yr^{-1}$ for Fe (Resing et al., 2015)). However, these estimates only took into account hot hydrothermal vent systems, and to our knowledge, no other dMn flux has been reported for low or moderately high temperature fluids. Manganese in seawater can be found as soluble Mn(II) or insoluble Mn(III) and Mn(IV), often as oxides and hydroxides (Sigel, 2000). Mn(II) has been shown to be rapidly oxidized and removed from the hydrothermal plume (Fitzsimmons et al., 2017; Resing et al., 2015), potentially by adsorption onto particles (Thibault de Chanvalon et al., 2023). In parallel, Mn(III) can be stabilized by organic ligands (Sigel, 2000). Organic ligands, present in the vicinity of the hydrothermal source, could further slow down manganese oxidation and precipitation in hydrothermal plumes, as shown for Fe and Cu (Sander and Koschinsky, 2011). A recent study showed that humic substances also play a major role in the stabilization of Mn(III), stabilizing 64% of the dMn (Thibault de Chanvalon et al., 2023). It also has been observed in a coastal area that 100% of the organic ligands complexing dMn were humic substances, which correspond to 86% of dMn stabilized by HS (Oldham et al., 2017). Although we do not have data for dMn eHS binding capacities in our study, this result appears to be of the same order of magnitude as dFe stabilization by eHS. This hypothesis, which remains to be verified, suggests that dMn could be stabilized as much as dFe close to hydrothermal sources. Where these hydrothermal inputs can reach the surface, they could be important not only for Fe, but also for Mn fertilization of Southern Ocean surface waters (Browning et al., 2021; Latour et al., 2021) and in shelf areas that see intrusions of this Fe- and Mn-enriched UCDW.

## 4. Conclusion

This new interdisciplinary study on the SWIR allowed us to highlight the presence of a hydrothermal plume in the vicinity of (−44.862°S; 36.174°E), characterized by low particulate materials, low dissolved Fe and Mn concentrations, high $CH_4$ concentrations and high $^{223}Ra$ and $^{224}Ra$ activities. The pFe and pMn concentrations were low, below 0.7 nmol $L^{-1}$ and 1.2 nmol $L^{-1}$, respectively, and very few oxyhydroxides were found, pointing to a probable low or moderately high temperature fluid hydrothermal source. Within the plume, dFe concentrations reached values up to 1.4 nmol $L^{-1}$. Electroactive HS had the estimated capacity to bind between 27 ± 6% and 60 ± 12% of dFe, if we assume that the Fe-binding capacity of hydrothermally sourced eHS is not different from the terrestrial standards used for their quantification. Other ligands not measured in this study may complex the remaining dFe; and/or a fraction of dFe could be under free cation form or inorganically complexed. The vertical diffusive fluxes of both dFe and dMn were estimated to be of equivalent magnitude (479 ± 281 nmol $m^{-2}$ $d^{-1}$ for dFe and 242 ± 64 nmol $m^{-2}$ $d^{-1}$ for dMn). However, although the system was shown to be a source of both dFe and dMn to the deep ocean, the low currents and the bathymetry likely limit the transport of this hydrothermal dFe and dMn input to the surface water to cause fertilization along this section of the SWIR. Further investigation remains to be done to precisely localize the hydrothermal source and to better characterize the exact nature of this source. Finally, future studies on the physical speciation and organic complexation of dMn emitted by hydrothermal vents will help to better constrain how hydrothermal sources may participate in fertilizing surface waters of HNLC areas.

## CRediT authorship contribution statement

**Corentin Baudet:** Conceptualization, Data curation, Formal analysis, Investigation, Methodology, Validation, Visualization, Writing – original draft, Writing – review & editing. **Eva Bucciarelli:** Conceptualization, Investigation, Methodology, Supervision, Writing – original draft, Writing – review & editing. **Géraldine Sarthou:** Conceptualization, Investigation, Methodology, Supervision, Validation, Writing – original draft, Writing – review & editing. **Cédric Boulart:** Data curation, Formal analysis, Writing – original draft. **Ewan Pelleter:** Conceptualization, Data curation, Formal analysis, Validation, Visualization, Writing – original draft, Writing – review & editing. **Millie Goddard-Dwyer:** Data curation, Formal analysis, Writing – original draft, Writing – review & editing. **Hannah Whitby:** Data curation, Methodology, Writing – original draft, Writing – review & editing. **Rui Zhang:** Data curation, Methodology. **Ingrid Obernosterer:** Methodology, Validation, Writing – original draft. **David Gonzalez-Santana:** Data curation, Formal analysis, Investigation. **Morgane Léon:** Data curation, Formal analysis, Investigation, Validation, Visualization, Writing – original draft, Writing – review & editing. **Pieter van Beek:** Data curation, Formal analysis, Investigation, Writing – original draft, Writing – review & editing. **Virginie Sanial:** Data curation, Formal analysis, Investigation, Methodology, Writing – original draft. **Catherine Jeandel:** Data curation, Investigation, Methodology, Writing – original draft. **Frédéric Vivier:** Data curation, Formal analysis, Investigation, Writing – original draft, Writing – review & editing. **Maria-Elena Vorrath:** Data curation, Writing – original draft. **Wen-Hsuan Liao:** Data curation, Formal analysis, Writing – original draft. **Yoan Germain:** Data curation, Formal analysis, Validation. **Hélène Planquette:** Conceptualization, Data curation, Formal analysis, Funding acquisition, Methodology, Project administration, Supervision, Validation, Visualization, Writing – original draft, Writing – review & editing.

## Declaration of competing interest

None.

## Data availability

Data will be made available on request.

## Acknowledgments

We would like to thank the captain A. Eyssautier, LDA and GENAVIR officers, engineers, technicians and the crew of the R/V Marion Dufresne for their enthusiasm and their professional assistance during the SWINGS cruise. The authors also thank Emmanuel de Saint-Léger and Fabien Pérault (CNRS DT INSU) for their help with the preparation, deployment and maintenance of the clean rosette. We thank Nolwenn Lemaitre and Bruno Hamelin for their help in the clean container. We are grateful to Gérard Eldin, Sara Sergi, Corentin Clerc, Lloyd Izard, and Elodie Kestenare for CTD data acquisition. We thank Anne Briais, Cyrille Poncelet, Carla Scalabrin, Hervé Bisquay, Cédric Cotté and Lloyd Izard for the hydrothermal survey. We also thank Alastair Lough and Shelby Gunnells for sharing their data gathered on the “Lost City” hydrothermal vent, and Erwan Roussel for fruitful discussions on microbiology. The SWINGS project was supported by the Flotte Océanographique Française (10.17600/18001925), Agence Nationale de la Recherche (ANR 19-CE01-0012), CNRS/ INSU (Centre National de la Recherche Scientifique/Institut National des Sciences de l’Univers) through its LEFE actions, Université de Bretagne Occidentale, and IsBlue project, Interdisciplinary graduate school for the blue planet (ANR 17-EURE-0015) and co-funded by a grant from the French government under the program ‘Investissements d’Avenir” embedded in France 2030.

## Appendix A. Supplementary data

Supplementary data to this article can be found online at https://doi.org/10.1016/j.marchem.2024.104401.

## References


Abualhaija, M.M., Whitby, H., van den Berg, C.M.G., 2015. Competition between copper and iron for humic ligands in estuarine waters. Mar. Chem. 172, 46–56. https://doi.org/10.1016/j.marchem.2015.03.010.

Ardyna, M., Lacour, L., Sergi, S., d'Ovidio, F., Sallée, J.-B., Rembauville, M., Blain, S., Tagliabue, A., Schlitzer, R., Jeandel, C., Arrigo, K.R., Claustre, H., 2019. Hydrothermal vents trigger massive phytoplankton blooms in the Southern Ocean. Nat. Commun. 10, 2451. https://doi.org/10.1038/s41467-019-09973-6.

Aumont, O., Bopp, L., 2006. Globalizing results from ocean in situ iron fertilization studies. Glob. Biogeochem. Cycles 20. https://doi.org/10.1029/2005GB002591.

Bach, W., Banerjee, N.R., Dick, H.J.B., Baker, E.T., 2002. Discovery of ancient and active hydrothermal systems along the ultra-slow spreading southwest Indian ridge 10°–16°E. Geochem. Geophys. Geosyst. 3, 1–14. https://doi.org/10.1029/2001GC000279.

Baker, E.T., 2017. Exploring the ocean for hydrothermal venting: new techniques, new discoveries, new insights. Ore Geol. Rev. 86, 55–69. https://doi.org/10.1016/j.oregeorev.2017.02.006.

Baker, E., Edmonds, H., Michael, P., Bach, W., Dick, H., Snow, J., Walker, S., Banerjee, N., Langmuir, C., 2004. Hydrothermal venting in magma deserts: the ultraslow-spreading Gakkel and Southwest Indian Ridges. Geochem. Geophys. Geosyst. 5 https://doi.org/10.1029/2004GC000712.

Beaulieu, S.E., Baker, E.T., German, C.R., 2015. Where are the undiscovered hydrothermal vents on oceanic spreading ridges? Deep Sea Research Part II: Topical Studies in Oceanography. Expl. New Front. Deep-Sea Res. Honor Memory Peter A. Rona 121, 202–212. https://doi.org/10.1016/j.dsr2.2015.05.001.

Bennett, S.A., Achterberg, E.P., Connelly, D.P., Statham, P.J., Fones, G.R., German, C.R., 2008. The distribution and stabilisation of dissolved Fe in deep-sea hydrothermal plumes. Earth Planet. Sci. Lett. 270, 157–167. https://doi.org/10.1016/j.epsl.2008.01.048.

Bolton, B.R., Both, R., Exon, N.F., Hamilton, T.F., Ostwald, J., Smith, J.D., 1988. Geochemistry and mineralogy of seafloor hydrothermal and hydrogenetic Mn oxide deposits from the Manus Basin and Bismarck archipelago region of the Southwest Pacific Ocean. Mar. Geol. 85, 65–87. https://doi.org/10.1016/0025-3227(88)90084-9.

Boyd, P.W., Ellwood, M.J., 2010. The biogeochemical cycle of iron in the ocean. Nat. Geosci. 3, 675–682. https://doi.org/10.1038/ngeo964.

Browning, T.J., Achterberg, E.P., Engel, A., Mawji, E., 2021. Manganese co-limitation of phytoplankton growth and major nutrient drawdown in the Southern Ocean. Nat. Commun. 12, 884. https://doi.org/10.1038/s41467-021-21122-6.

Cannat, M., Mahato, S., Martinez, I., Frueh-Green, G., Bernasconi, S., Lecoeuvre, A., Vitale Brovarone, A., Brunelli, D., Fontaine, F., Prampolini, M., Agrinier, P., Bickert, M., Hamelin, C., Lie Onstad, S., Maia, M., Roumejon, S., 2021. Carbonate-Brucite Chimneys At The Southwest Indian Ridge: The Old City Hydrothermal Field, 2021, pp. V33A–09.

Cathalot, C., Roussel, E.G., Perhirin, A., Creff, V., Donval, J.-P., Guyader, V., Roullet, G., Gula, J., Tamburini, C., Garel, M., Godfroy, A., Sarradin, P.-M., 2021. Hydrothermal plumes as hotspots for deep-ocean heterotrophic microbial biomass production. Nat. Commun. 12, 6861. https://doi.org/10.1038/s41467-021-26877-6.

Cave, R., German, C., Thomson, J., Nesbitt, R., 2002. Fluxes to sediments underlying the rainbow hydrothermal plume at 36°14′N on the mid-Atlantic ridge. Geochim. Cosmochim. Acta 66, 1905–1923. https://doi.org/10.1016/S0016-7037(02)00823-2.

Charlou, J.-L., Bougault, H., Fouquet, Y., Donval, J.-P., Douville, E., Knoery, J., Aballéa, M., Needham, H.D., Jean-Baptiste, P., Rona, P., Langmuir, C., German, C., 1996. Methane Degassing, Hydrothermal Activity and Serpentinization between the Fifteen-Twenty Fracture Zone Area and the Azores Triple Junction Area (Mid-Atlantic Ridge).

Charlou, J.-L., Donval, J.P., Fouquet, Y., Jean-Baptiste, P., Holm, N., 2002. Charlou J-L, Donval J-P, Fouquet Y, Jean-Baptiste P, Holm N. Geochemistry of high H2 and CH4 vent fluids issuing from ultramafic rocks at the rainbow hydrothermal field (36°14′N, MAR). Chem Geol 191: 345-359. Chem. Geol. 191, 345–359. https://doi.org/10.1016/S0009-2541(02)00134-1.

Corliss, J.B., Dymond, J., Gordon, L.I., Edmond, J.M., von Herzen, R.P., Ballard, R.D., Green, K., Williams, D., Bainbridge, A., Crane, K., van Andel, T.H., 1979. Submarine thermal springs on the Galápagos rift. Science 203, 1073–1083. https://doi.org/10.1126/science.203.4385.1073.

Cutter, G., Casciotti, K., Croot, P., Geibert, W., Heimbürger, L.-E., Lohan, M., Planquette, H., van de Flierdt, T., 2017. Sampling and Sample-handling Protocols for GEOTRACES Cruises. Version 3, August 2017. (Report). GEOTRACES International Project Office.

Debeljak, P., Blain, S., Bowie, A., van der Merwe, P., Bayer, B., Obernosterer, I., 2021. Homeostasis drives intense microbial trace metal processing on marine particles. Limnol. Oceanogr. 66, 3842–3855. https://doi.org/10.1002/lno.11923.

Diehl, A., Bach, W., 2020. MARHYS (MARine HYdrothermal solutions) database: a global compilation of marine hydrothermal vent fluid, end member, and seawater compositions. Geochem. Geophys. Geosyst. 21, e2020GC009385 https://doi.org/10.1029/2020GC009385.

Fang, Z., Wang, W.-X., 2021. Size speciation of dissolved trace metals in hydrothermal plumes on the southwest Indian ridge. Sci. Total Environ. 771, 145367 https://doi.org/10.1016/j.scitotenv.2021.145367.

Fitzsimmons, J.N., Boyle, E.A., Jenkins, W.J., 2014. Distal transport of dissolved hydrothermal iron in the deep South Pacific Ocean. PNAS 111, 16654–16661. https://doi.org/10.1073/pnas.1418778111.

Fitzsimmons, J.N., John, S.G., Marsay, C.M., Hoffman, C.L., Nicholas, S.L., Toner, B.M., German, C.R., Sherrell, R.M., 2017. Iron persistence in a distal hydrothermal plume supported by dissolved–particulate exchange. Nat. Geosci. 10, 195–201. https://doi.org/10.1038/ngeo2900.

Fouquet, Y., Cambon, P., Etoubleau, J., Charlou, J.-L., Ondreas, H., Barriga, F., Cherkashov, G., Semkova, T., Poroshina, I., Bohn, M., Donval, J.P., Henry, K., Murphy, P., Rouxel, O., 2010. Geodiversity of hydrothermal processes along the mid-Atlantic ridge and ultramafic-hosted mineralization: a new type of oceanic Cu-Zn-Co-Au volcanogenic massive sulfide deposit. Washington DC Am. Geophys. Union Geophys. Monograph Series 188, 321–367. https://doi.org/10.1029/2008GM000746.

Gartman, A., Findlay, A., 2020. Impacts of hydrothermal plume processes on oceanic metal cycles and transport. Nat. Geosci. 13, 1–7. https://doi.org/10.1038/s41561-020-0579-0.

German, C.R., Seyfried, W.E., 2014. Hydrothermal processes. In: Treatise on Geochemistry. Elsevier, pp. 191–233. https://doi.org/10.1016/B978-0-08-095975-7.00607-0.

German, C., Baker, E., Mevel, C., Tamaki, K., Blondel, P., Evans, A., Flewellen, C., Matthew, D., Parson, L., Sauter, D., Fujimoto, H., Osada, Y., Tamura, C., Yamashi, T., Gomez, O., Lee, S.-M., Searle, R., Patriat, P., Pouliquen, G., Yamada, T., 1998. Hydrothermal activity along the southwest Indian ridge. Nature 395, 490–493. https://doi.org/10.1038/26730.

German, C.R., Thurnherr, A.M., Knoery, J., Charlou, J.-L., Jean-Baptiste, P., Edmonds, H. N., 2010. Heat, volume and chemical fluxes from submarine venting: a synthesis of results from the rainbow hydrothermal field, 36°N MAR. Deep-Sea Res. I Oceanogr. Res. Pap. 57, 518–527. https://doi.org/10.1016/j.dsr.2009.12.011.

German, C.R., Reeves, E.P., Türke, A., Diehl, A., Albers, E., Bach, W., Purser, A., Ramalho, S.P., Suman, S., Mertens, C., Walter, M., Ramirez-Llodra, E., Schlindwein, V., Bünz, S., Boetius, A., 2022. Volcanically hosted venting with indications of ultramafic influence at Aurora hydrothermal field on Gakkel ridge. Nat. Commun. 13, 6517. https://doi.org/10.1038/s41467-022-34014-0.

González-Santana, D., Planquette, H., Cheize, M., Whitby, H., Gourain, A., Holmes, T., Guyader, V., Cathalot, C., Pelleter, E., Fouquet, Y., Sarthou, G., 2020. Processes driving iron and manganese dispersal from the TAG hydrothermal plume (Mid-Atlantic Ridge): Results from a GEOTRACES process study. Front. Mar. Sci. 7.

Gordon, A.L., 1975. An Antarctic oceanographic section along 170°E. Deep-Sea Res. Oceanogr. Abstr. 22, 357–377. https://doi.org/10.1016/0011-7471(75)90060-1.

Han, X., Wu, G., Cui, R., Qiu, Z., Deng, X., Wang, Y., 2010. Scientific Party Of Dy115–21 Cruise Leg 7. In: Discovery of a Hydrothermal Sulfide Deposit on the Southwest Indian Ridge at 49.2°E 2010, OS21C-1531.

Hassler, C.S., van den Berg, C.M.G., Boyd, P.W., 2017. Toward a regional classification to provide a more inclusive examination of the ocean biogeochemistry of iron-binding ligands. Front. Mar. Sci. 4.

Hawkes, J.A., Connelly, D.P., Gledhill, M., Achterberg, E.P., 2013. The stabilisation and transportation of dissolved iron from high temperature hydrothermal vent systems. Earth Planet. Sci. Lett. 375, 280–290. https://doi.org/10.1016/j.epsl.2013.05.047.

Hawkes, J.A., Connelly, D.P., Rijkenberg, M.J.A., Achterberg, E.P., 2014. The importance of shallow hydrothermal island arc systems in ocean biogeochemistry. Geophys. Res. Lett. 41, 942–947. https://doi.org/10.1002/2013GL058817.

Henderson, P.B., Morris, P.J., Moore, W.S., Charette, M.A., 2013. Methodological advances for measuring low-level radium isotopes in seawater. J. Radioanal. Nucl. Chem. 296, 357–362. https://doi.org/10.1007/s10967-012-2047-9.

Hoffman, C.L., Monreal, P.J., Albers, J.B., Lough, A.J.M., Santoro, A.E., Mellett, T., Buck, K.N., Tagliabue, A., Lohan, M.C., Resing, J.A., Bundy, R.M., 2023. Microbial Siderophore Production is Tightly Coupled to Iron in Hydrothermal Plumes. https://doi.org/10.1101/2023.01.05.522639.

Humler, 2001. MD 121 / SWIFT cruise, Marion Dufresne R/V. https://doi.org/10.17600/1200030.

Kolb, B., Ettre, L.S., 1997. Static Headspace-Gas Chromatography: Theory and Practice, 2nd Edition | Wiley [WWW Document]. Wiley.com. URL https://www.wiley.com/en-us/Static+Headspace+Gas+Chromatography%3A+Theory+and+Practice%2C+2nd+Edition-p-9780471749448 (accessed 3.8.23).

Konn, C., Charlou, J.L., Donval, J.P., Holm, N.G., Dehairs, F., Bouillon, S., 2009. Hydrocarbons and oxidized organic compounds in hydrothermal fluids from rainbow and lost City ultramafic-hosted vents. Chem. Geol. 258, 299–314. https://doi.org/10.1016/j.chemgeo.2008.10.034.

Laglera, L.M., van den Berg, C.M.G., 2009. Evidence for geochemical control of iron by humic substances in seawater. Limnol. Oceanogr. 54, 610–619. https://doi.org/10.4319/lo.2009.54.2.0610.

Latour, P., Wuttig, K., van der Merwe, P., Strzepek, R.F., Gault-Ringold, M., Townsend, A. T., Holmes, T.M., Corkill, M., Bowie, A.R., 2021. Manganese biogeochemistry in the Southern Ocean, from Tasmania to Antarctica. Limnol. Oceanogr. 66, 2547–2562. https://doi.org/10.1002/lno.11772.

Lecoeuvre, A., Ménez, B., Cannat, M., Chavagnac, V., Gérard, E., 2021. Microbial ecology of the newly discovered serpentinite-hosted Old City hydrothermal field (southwest Indian ridge). ISME J. 15, 818–832. https://doi.org/10.1038/s41396-020-00816-7.

Léon, M., van Beek, P., Sanial, V., Baudet, C., Charette, A., Souhaut, M., Vivier, F., Kestenare, E., Jeandel, C., Planquette, H., 2024. Investigation of hydrothermal activity in the South West Indian Ridge region using Ra isotopes and $^{227}$Ac as tracers. Prog. Oceanogr. 103191.

Lough, A.J.M., Tagliabue, A., Demasy, C., Resing, J.A., Mellett, T., Wyatt, N.J., Lohan, M. C., 2023. Tracing differences in iron supply to the mid-Atlantic ridge valley between hydrothermal vent sites: implications for the addition of iron to the deep ocean. Biogeosciences 20, 405–420. https://doi.org/10.5194/bg-20-405-2023.

Love, B.A., Resing, J.A., Cowen, J.P., Lupton, J.E., Fornari, D.J., Shank, T.M., Biller, D., 2008. Methane, manganese, and helium in hydrothermal plumes following volcanic eruptions on the East Pacific rise near 9°50′N. Geochem. Geophys. Geosyst. 9 https://doi.org/10.1029/2008GC002104.

Luther, G.W., Kostka, J.E., Church, T.M., Sulzberger, B., Stumm, W., 1992. Seasonal iron cycling in the salt-marsh sedimentary environment: the importance of ligand complexes with Fe(II) and Fe(III) in the dissolution of Fe(III) minerals and pyrite, respectively. Marine Chem. Prog. Marine Chem. 40, 81–103. https://doi.org/10.1016/0304-4203(92)90049-G.

Martin, W., Baross, J., Kelley, D., Russell, M.J., 2008. Hydrothermal vents and the origin of life. Nat. Rev. Microbiol. 6, 805–814. https://doi.org/10.1038/nrmicro1991.

Moorby, S.A., Cronan, D.S., Glasby, G.P., 1984. Geochemistry of hydrothermal Mn-oxide deposits from the S.W. Pacific island arc. Geochim. Cosmochim. Acta 48, 433–441. https://doi.org/10.1016/0016-7037(84)90272-2.

Moore, W.S., 2008. Fifteen years experience in measuring 224Ra and 223Ra by delayed coincidence counting. Mar. Chem. 109, 188–197. https://doi.org/10.1016/j.marchem.2007.06.015.

Moore, J.K., Braucher, O., 2008. Sedimentary and mineral dust sources of dissolved iron to the world ocean. Biogeosciences 5, 631–656.

Moreau, S., Hattermann, T., de Steur, L., Kauko, H.M., Ahonen, H., Ardelan, M., Assmy, P., Chierici, M., Descamps, S., Dinter, T., Falkenhaug, T., Fransson, A., Grønningsæter, E., Hallfredsson, E.H., Huhn, O., Lebrun, A., Lowther, A., Lübcker, N., Monteiro, P., Peeken, I., Roychoudhury, A., Różańska, M., Ryan-Keogh, T., Sanchez, N., Singh, A., Simonsen, J.H., Steiger, N., Thomalla, S.J., van Tonder, A., Wiktor, J.M., Steen, H., 2023. Wind-driven upwelling of iron sustains dense blooms and food webs in the eastern Weddell gyre. Nat. Commun. 14, 1303. https://doi.org/10.1038/s41467-023-36992-1.

Morton, P.L., Landing, W.M., Hsu, S.C., Milne, A., Aguilar-Islas, A.M., Baker, A.R., Zamora, L.M., 2013. Methods for the sampling and analysis of marine aerosols: results from the 2008 GEOTRACES aerosol intercalibration experiment. Limnol. Oceanogr.: Methods 11 (2), 62–78.

Murphy, E., McMurtry, G.M., Kim, K.H., DeCarlo, E.H., 1991. Geochemistry and geochronology of a hydrothermal ferromanganese deposit from the North Fiji Basin. Marine Geol. Geol. Geophys. Min. Res. South Pacific 98, 297–312. https://doi.org/10.1016/0025-3227(91)90108-G.

Nadeau, K., Brophy, C., Yang, L., Grinberg, P., Pihillagawa Gedara, I., Meija, J., Pagliano, E., McRae, G., Mester, Z., 2016. NASS-7: Seawater Certified Reference Material for Trace Metals and Other Constituents. https://doi.org/10.4224/crm.2016.nass-7.

Oldham, V.E., Mucci, A., Tebo, B.M., Luther, G.W., 2017. Soluble Mn(III)–L complexes are abundant in oxygenated waters and stabilized by humic ligands. Geochim. Cosmochim. Acta 199, 238–246. https://doi.org/10.1016/j.gca.2016.11.043.

Omanovic, D., Pizeta, I., 2016. High Frequncy data tratment andd visualization with ECDSOFT and OnLineMonitor. In: Obrador, B., Jones, I.D., Jennings, E.D. (Eds.), NETLAKE toolbox for tthe analysis of high frequency data from lakes (Factsheet 5).

Palleroni, N.J., 2015. Burkholderia, in: Bergey's Manual of Systematics of Archaea and Bacteria. John Wiley & Sons, Ltd, pp. 1–50. https://doi.org/10.1002/9781118960608.gbm00935.

Park, Y.-H., Park, T., Kim, T.-W., Lee, S.-H., Hong, C.-S., Lee, J.-H., Rio, M.-H., Pujol, M.-I., Ballarotta, M., Durand, I., Provost, C., 2019. Observations of the Antarctic circumpolar current over the Udintsev fracture zone, the narrowest choke point in the Southern Ocean. J. Geophys. Res. Oceans 124, 4511–4528. https://doi.org/10.1029/2019JC015024.

Pernet-Coudrier, B., Waeles, M., Filella, M., Quentel, F., Riso, R.D., 2013. Simple and simultaneous determination of glutathione, thioacetamide and refractory organic matter in natural waters by DP-CSV. Sci. Total Environ. 463–464, 997–1005. https://doi.org/10.1016/j.scitotenv.2013.06.053.

Piola, A.R., Georgi, D.T., 1982. Circumpolar properties of Antarctic intermediate water and Subantarctic mode water. Deep Sea Res. Part A. Ocean. Res. Papers 29, 687–711. https://doi.org/10.1016/0198-0149(82)90002-4.

Planquette, H., Sherrell, R.M., 2012. Sampling for particulate trace element determination using water sampling bottles: methodology and comparison to in situ pumps. Limnol. Oceanogr. Methods 10, 367–388. https://doi.org/10.4319/lom.2012.10.367.

Ray, D., Kamesh Raju, K.A., Baker, E.T., Srinivas Rao, A., Mudholkar, A.V., Lupton, J.E., Vijaya Kumar, T., 2012. Hydrothermal plumes over th Carlsberg Ridge, Indian Ocean. Geochem. Geophys. Geosystems 13 (1).

Reeburgh, W.S., 2007. Oceanic methane biogeochemistry. Chem. Rev. 107, 486–513. https://doi.org/10.1021/cr050362v.

Resing, J.A., Sedwick, P.N., German, C.R., Jenkins, W.J., Moffett, J.W., Sohst, B.M., Tagliabue, A., 2015. Basin-scale transport of hydrothermal dissolved metals across the South Pacific Ocean. Nature 523, 200–203. https://doi.org/10.1038/nature14577.

Rintoul, S.R., 2018. The global influence of localized dynamics in the Southern Ocean. Nature 558, 209–218. https://doi.org/10.1038/s41586-018-0182-3.

Roshan, S., DeVries, T., Wu, J., John, S., Weber, T., 2020. Reversible scavenging traps hydrothermal iron in the deep ocean. Earth Planet. Sci. Lett. 542, 116297 https://doi.org/10.1016/j.epsl.2020.116297.

Sander, S.G., Koschinsky, A., 2011. Metal flux from hydrothermal vents increased by organic complexation. Nat. Geosci. 4, 145–150. https://doi.org/10.1038/ngeo1088.

Sands, C.M., Connelly, D.P., Statham, P.J., German, C.R., 2012. Size fractionation of trace metals in the Edmond hydrothermal plume, Central Indian Ocean. Earth Planet. Sci. Lett. 319–320, 15–22. https://doi.org/10.1016/j.epsl.2011.12.031.

Sarma, N.S., Kiran, R., Rama Reddy, M., Iyer, S.D., Peketi, A., Borole, D.V., Krishna, M.S., 2018. Hydrothermal alteration promotes humic acid formation in sediments: a case study of the Central Indian Ocean Basin. J. Geophys. Res. Oceans 123, 110–130. https://doi.org/10.1002/2017JC012940.

Sato, T., Okino, K., Sato, H., Mizuno, M., Hanyu, T., Seama, N., 2013. Magmatic activities on the southwest Indian ridge between 35°E and 40°E, the closest segment to the Marion hotspot. Geochem. Geophys. Geosyst. 14, 5286–5307. https://doi.org/10.1002/2013GC004814.

Sauter, D., Cannat, M., 2010. The ultraslow spreading southwest Indian ridge. In: Rona, P.A., Devey, C.W., Dyment, J., Murton, B.J. (Eds.), Geophysical Monograph Series. American Geophysical Union, Washington, D. C, pp. 153–173. https://doi.org/10.1029/2008GM000843.

Schine, C.M.S., Alderkamp, A.-C., van Dijken, G., Gerringa, L.J.A., Sergi, S., Laan, P., van Haren, H., van de Poll, W.H., Arrigo, K.R., 2021. Massive Southern Ocean phytoplankton bloom fed by iron of possible hydrothermal origin. Nat. Commun. 12, 1211. https://doi.org/10.1038/s41467-021-21339-5.

Shock, E.L., 1992. Chemical environments of submarine hydrothermal systems. In: Holm, N.G. (Ed.), Marine Hydrothermal Systems and the Origin of Life: Report of SCOR Working Group 91. Springer, Netherlands, Dordrecht, pp. 67–107. https://doi.org/10.1007/978-94-011-2741-7_5.

Sigel, 2000. Metal ions in biological systems. In: Manganese and its Role in Biological Processes [WWW Document], Vol. 37. Routledge & CRC Press. URL https://www.routledge.com/Metal-Ions-in-Biological-Systems-Volume-37-Manganese-and-Its-Role-in-Biological/Sigel/p/book/9780367398934 (accessed 3.15.23).

Sukekava, C., Downes, J., Slagter, H.A., Gerringa, L.J.A., Laglera, L.M., 2018. Determination of the contribution of humic substances to iron complexation in seawater by catalytic cathodic stripping voltammetry. Talanta 189, 359–364. https://doi.org/10.1016/j.talanta.2018.07.021.

Sunda, W., 2012. Feedback interactions between trace metal nutrients and phytoplankton in the ocean. Front. Microbiol. 3 https://doi.org/10.3389/fmicb.2012.00204.

Tagliabue, A., Resing, J., 2016. Impact of hydrothermalism on the ocean iron cycle. Philos. Trans. R. Soc. A Math. Phys. Eng. Sci. 374, 20150291. https://doi.org/10.1098/rsta.2015.0291.

Tagliabue, A., Mtshali, T., Aumont, O., Bowie, A.R., Klunder, M.B., Roychoudhury, A.N., Swart, S., 2012. A global compilation of dissolved iron measurements: focus on distributions and processes in the Southern Ocean. Biogeosciences 9, 2333–2349. https://doi.org/10.5194/bg-9-2333-2012.

Tagliabue, A., Bowie, A.R., Boyd, P.W., Buck, K.N., Johnson, K.S., Saito, M.A., 2017. The integral role of iron in ocean biogeochemistry. Nature 543, 51–59. https://doi.org/10.1038/nature21058.

Tagliabue, A., Lough, A.J.M., Vic, C., Roussenov, V., Gula, J., Lohan, M.C., Resing, J.A., Williams, R.G., 2022. Mechanisms driving the dispersal of hydrothermal iron from the Northern Mid Atlantic Ridge. Geophys. Res. Lett. 49, e2022GL100615 https://doi.org/10.1029/2022GL100615.

Tao, C., Wu, G., Ni, J., Zhao, H., Su, X., Zhou, N., Li, J., Chen, Y., Cui, R., Deng, X., Egorov, I., Dobretsova, I., Sun, G., Qiu, Z., Zhou, J., Gu, C., Yang, J., Zhang, K., Wu, X., Lin, J., 2009. New hydrothermal fields found along the SWIR during the Legs 5-7 of the Chinese DY115-20 Expedition. In: AGU Fall Meeting Abstracts, 1150.

Tao, C., Lin, J., Guo, S., Chen, Y.J., Wu, G., Han, X., German, C.R., Yoerger, D.R., Zhou, N., Li, H., Su, X., Zhu, J., the DY115-19 (Legs 1–2) and DY115-20 (Legs 4–7) Science Parties, 2012. First active hydrothermal vents on an ultraslow-spreading center: Southwest Indian Ridge. Geology 40, 47–50. https://doi.org/10.1130/G32389.1.

Tao, C., Li, H., Zhou, J., Wu, T., He, Y., Deng, X., Zhang, G., Liu, W., 2014. Seafloor hydrothermal activity and polymetallic sulfide exploration on the southwest Indian ridge. Chin. Sci. Bull. 59, 2266–2276. https://doi.org/10.1007/s11434-014-0182-0.

Thibault de Chanvalon, A., Luther III, G.W., Oldham, V.E., Tebo, B.M., Coffey, N.R., Shaw, T.F., 2023. Distribution and stability of Mn complexes in the ocean: influence of hydrothermal plumes and weather events. Limnol. Oceanogr. 68, 455–466. https://doi.org/10.1002/lno.12285.

Tonnard, M., Planquette, H., Bowie, A.R., van der Merwe, P., Gallinari, M., Desprez de Gésincourt, F., Germain, Y., Gourain, A., Benetti, M., Reverdin, G., Tréguer, P., Boutorh, J., Cheize, M., Lacan, F., Menzel Barraqueta, J.-L., Pereira-Contreira, L., Shelley, R., Lherminier, P., Sarthou, G., 2020. Dissolved iron in the North Atlantic Ocean and Labrador Sea along the GEOVIDE section (GEOTRACES section GA01). Biogeosciences 17, 917–943. https://doi.org/10.5194/bg-17-917-2020.

Usui, A., Yuasa, M., Yokota, S., Nohara, M., Nishimura, A., Murakami, F., 1986. Submarine hydrothermal manganese deposits from the Ogasawara (Bonin) Arc, off the Japan Islands. Mar. Geol. 73, 311–322. https://doi.org/10.1016/0025-3227(86)90020-4.

van Hulten, M.M.P., Middag, R., Dutay, J.-C., de Baar, H.J.W., Roy-Barman, M., Gehlen, M., Tagliabue, A., Sterl, A., 2017. Manganese in the West Atlantic Ocean in context of the first global ocean circulation model of manganese. Biogeosciences 14, 1123–1152. https://doi.org/10.5194/bg-14-1123-2017.

Von Damm, K.L., 1990. Seafloor hydrothermal activity: black smoker chemistry and chimneys. Annu. Rev. Earth Planet. Sci. 18, 173–204. https://doi.org/10.1146/annurev.ea.18.050190.001133.

Wang, H., Yan, Q., Yang, Q., Ji, F., Wong, K.H., Zhou, H., 2019. The size fractionation and speciation of iron in the Longqi hydrothermal plumes on the Southwest Indian Ridge. J. Geophys. Res. Oceans 124, 4029–4043. https://doi.org/10.1029/2018JC014713.

Wheat, C.G., Feely, R.A., Mottl, M.J., 1996. Phosphate removal by oceanic hydrothermal processes: an update of the phosphorus budget in the oceans. Geochim. Cosmochim. Acta 60, 3593–3608. https://doi.org/10.1016/0016-7037(96)00189-5.

Whitby, H., van den Berg, C.M.G., 2015. Evidence for copper-binding humic substances in seawater. In: Marine Chemistry, SCOR WG 139: Organic Ligands – A Key Control on Trace Metal Biogeochemistry in the Ocean, 173, pp. 282–290. https://doi.org/10.1016/j.marchem.2014.09.011.

Whitby, H., Planquette, H., Cassar, N., Bucciarelli, E., Osburn, C.L., Janssen, D.J., Cullen, J.T., González, A.G., Völker, C., Sarthou, G., 2020. A call for refining the role of humic-like substances in the oceanic iron cycle. Sci. Rep. 10, 6144. https://doi.org/10.1038/s41598-020-62266-7.

Willie, S., Boyko, V., Brophy, C., Clancy, V., Pihillagawa Gedara, I., Grinberg, P., Kumkrong, P., Mercier, P.H.J., Mihai, O., Tyo, D.D., Jiang, C., Kingston, D.M., Maxwell, P., Meija, J., Mester, Z., Sturgeon, R., Yang, L., 2013. PACS-3: Marine Sediment Certified Reference Material for Total and Extractable Metal Content. https://doi.org/10.4224/crm.2013.pacs-3.

Willie, S., Nadeau, K., Pihillagawa Gedara, I., Yang, L., Clancy, V., Grinberg, P., Kumkrong, P., Mercier, P.H.J., Mihai, O., Tyo, D.D., Jiang, C., Kingston, D.M., Meija, J., Maxwell, P., Mester, Z., 2014. MESS-4: Marine Sediment Certified Reference Material for Total and Extractable Metal Content. https://doi.org/10.4224/crm.2014.mess-4.

Wong, A., 2005. Subantarctic mode water and Antarctic intermediate water in the South Indian Ocean based on profiling float data 20002004. J. Mar. Res. 63, 789–812. https://doi.org/10.1357/0022240054663196.

Yamashita, Y., Nishioka, J., Obata, H., Ogawa, H., 2020. Shelf humic substances as carriers for basin-scale iron transport in the North Pacific. Sci. Rep. 10, 4505. https://doi.org/10.1038/s41598-020-61375-7.

Yücel, M., Gartman, A., Chan, C.S., Luther, G.W., 2011. Hydrothermal vents as a kinetically stable source of iron-sulphide-bearing nanoparticles to the ocean. Nat. Geosci. 4, 367–371. https://doi.org/10.1038/ngeo1148.

Zhou, H., Dick, H.J.B., 2013. Thin crust as evidence for depleted mantle supporting the Marion rise. Nature 494, 195–200. https://doi.org/10.1038/nature11842.

Zu, Y., Gao, L., Guo, G., Fang, Y., 2022. Changes of circumpolar deep water between 2006 and 2020 in the south-West Indian Ocean, East Antarctica. Deep-Sea Res. II Top. Stud. Oceanogr. 197, 105043 https://doi.org/10.1016/j.dsr2.2022.105043.